`Chronostar`: a novel Bayesian method for kinematic age determination − I. Derivation and application to the *β* Pictoris moving group

Timothy D. Crundall [ID],[1,2]★ Michael J. Ireland [ID],[1] Mark R. Krumholz [ID],[1,3]
Christoph Federrath,[1,3] Maruša Žerjal [ID][1] and Jonah T. Hansen[1]

[1]*Research School of Astronomy and Astrophysics, Australian National University, Canberra 2600, Australia*
[2]*Physikalisches Institut, Universität zu Köln, Zülpicher Str. 77, D-50937 Köln, Germany*
[3]*ARC Centre of Excellence for Astronomy in Three Dimensions (ASTRO-3D), Australia*

ABSTRACT

Gaia DR2 provides an unprecedented sample of stars with full 6D phase-space measurements, creating the need for a self-consistent means of discovering and characterizing the phase-space overdensities known as *moving groups* or *associations*. Here we present `Chronostar`, a new Bayesian analysis tool that meets this need. `Chronostar` uses the Expectation–Maximization algorithm to remove the circular dependency between association membership lists and fits to their phase-space distributions, making it possible to discover unknown associations within a kinematic data set. It uses forward-modelling of orbits through the Galactic potential to overcome the problem of tracing backward stars whose kinematics have significant observational errors, thereby providing reliable ages. In tests using synthetic data sets with realistic measurement errors and complex initial distributions, `Chronostar` successfully recovers membership assignments and kinematic ages up to ≈100 Myr. In tests on real stellar kinematic data in the phase-space vicinity of the *β* Pictoris Moving Group, `Chronostar` successfully rediscovers the association without any human intervention, identifies 10 new likely members, corroborates 48 candidate members, and returns a kinematic age of 17.8 ± 1.2 Myr. In the process we also rediscover the Tucana-Horologium Moving Group, for which we obtain a kinematic age of $36.3^{+1.3}_{-1.4}$ Myr.

Key words: methods: statistical – stars: kinematics and dynamics – stars: statistics – galaxy: kinematics and dynamics – open clusters and associations: general.

1 INTRODUCTION

With the advent of *Gaia* DR2 (Gaia Collaboration 2018) we have access to an all-sky, magnitude complete survey that provides full 6D kinematic information for over 7 000 000 stars. Within this wealth of data reside the kinematic fingerprints of star formation events in the form of moving groups, stars that were formed in close proximity (both spatially and temporally) that have since become unbound and are now following approximately ballistic trajectories through the Galaxy. The development of an accurate and reliable method to infer the origin site of a moving group is a critical step in using kinematic information to constrain stellar ages, which in turn would allow calibration of model-dependent ageing techniques. Accurate ages are important for many applications. They set the clock for circumstellar disc evolution and planet formation. Exoplanets are most easily directly imaged when they are young, so accurate ages enable better target selection for direct

imaging campaigns. Accurate ages are required for calibration of massive stellar evolution models, but are nearly impossible to obtain directly due to these stars' short Kelvin–Helmholtz contraction times; however, they can be age-dated approximately via their association with less massive members of a moving group.

However, current kinematic analysis methods have proven unable to deliver age estimates that are consistent with one another, or with other age estimators. One common kinematic approach is to estimate a *traceback age* by following the orbits of group members backwards through time to identify the age at which they occupied the smallest spatial volume. Ducourant et al. (2014) employ this technique to obtain a kinematic age for the TW Hydrae Association (TWA) of 7.5 ± 0.7 Myr. However Donaldson et al. (2016) obtain a different age of 3.8 ± 1.1 Myr using the same method, a discrepancy that they attribute to Ducourant et al. not properly propagating measurement uncertainties. Mamajek & Bell (2014) review age estimates for the *β* Pictoris Moving Group (henceforth *β*PMG) and find that traceback ages (Ortega et al. 2002; Song, Zuckerman & Bessell 2003, Ortega et al. 2004) are 4*σ*-discrepant with the combined lithium depletion boundary (LDB) and isochronal age of

★ E-mail: timothy.crundall@anu.edu.au

23 ± 3 Myr; the sole exception is the traceback age of 22 ± 12 Myr determined by Makarov (2007), which has such a large uncertainty that it provides little discriminatory power.

An alternative kinematic estimator is the *expansion age*, which one determines using a method analogous to the measurement of Hubble flow: one plots the positions of stars against their velocities in the same direction. If the stars are expanding, their positions and velocities will be correlated, and the slope of the correlation is just the inverse of the time since expansion began. Torres et al. (2006) apply this method to the X positions and velocities of βPMG stars to obtain an age of ~ 18 Myr.[1] While this is less than 2σ from the combined LDB and isochronal age of 23 ± 3 Myr, Mamajek & Bell (2014) point out that the expansion slope is not consistent across dimensions. Indeed performing the same analysis in the Z direction yields a negative slope, implying contraction rather than expansion.

The problems in current kinematic techniques likely have two distinct causes. First, the methods are not robust when applied to moving groups whose origin sites have complex structures in space or time. For example, Wright & Mamajek (2018) investigate the expansion rate of the Scorpius-Centaurus OB Association (Sco-Cen hereafter) by assuming it could be decomposed into three distinct subgroups (despite evidence that the true structure is significantly more complex; e.g. Rizzuto, Ireland & Kraus 2015), but find that the kinematics are more consistent with contraction than expansion, so that any expansion or traceback age one might derive is meaningless. Even in cases where stars are expanding, both traceback and expansion methods are likely to yield misleading results if there is a non-negligible spread in the spatial distribution or age of formation sites.

A second problem is membership determination. In order to apply a kinematic ageing technique to a moving group, one must start with a list of its members, constructed either by hand or using an automated tool such as LACEwING (Riedel et al. 2017) or BANYAN (Gagné et al. 2018b) that assigns membership probabilities based on fits in 3D position or 6D phase space. Using hand-selected membership lists often produces results that depend significantly on which stars are included. However, with the automated methods the process is somewhat circular: the centre and dispersion of a purported moving group depends on which stars are included as probable members, but which stars are included in turn depends on the adopted centre and dispersion of the group. When one attempts a kinematic traceback using member lists determined in this fashion, the errors compound to the point where the method is not viable. Riedel et al. (2017) find that they cannot determine kinematic ages for any known association, or even for a synthetic association described by a single age and a Gaussian distribution in space.

In this paper we introduce a new method called `Chronostar` that addresses many of the problems discussed above. Compared to existing methods, `Chronostar` has several advantages: (1) it simultaneously and self-consistently solves the problems of

membership determination and kinematic ageing; (2) it does not assume or require that moving groups have a single, simple origin in space and time, and thus allows for a more realistic representation of the complex structure of star-forming regions; (3) it uses forward modelling rather than traceback, thereby eliminating the need for complex and uncertain propagation of observational errors. Our layout for the remainder of this paper is as follows. We present the formal derivation of our method in Section 2, and in Section 3 we test it on a variety of synthetic data sets, demonstrating that it is both robust and accurate. In Section 4 we present a simple application to the β Pictoris Moving Group, showing that, for the first time, we are able to recover a kinematic age with tight error bars that is consistent with ages derived from other methods. We discuss `Chronostar`'s performance in comparison with other methods in Section 5. Finally, we summarize and discuss future prospects for our method in Section 6. The code for `Chronostar` can be found at https://github.com/mikeireland/chronostar.

2 METHODS

2.1 Setup

Our ultimate goal is to find the most likely kinematic description of an association's origin, such that evolving it through time by its modelled age to its *current-day* distribution, best explains the observed kinematic distribution of the association's members. In this section we detail our Bayesian approach to finding the best kinematic description of a stellar association by modelling its origins as the sum of Gaussians in 6D Cartesian phase-space with independent ages, means, and covariance matrices. We refer to each Gaussian as a *component*,[2] and for the simplified models presented here, each component has the same standard deviation in each position dimension, and the same standard deviation in each velocity dimension. We define the origin of an association as the point in time at which stars become gravitationally unbound and begin moving ballistically through the Galaxy. We approximate the initial positions and velocities to be uncorrelated with one another, but as the association evolves in time those quantities will become correlated – consequently the covariance matrix, and in particular the terms within it describing position-velocity covariance, are functions of time. We fit these components to a set of observed stars by maximizing the overlap between the observed stellar position-velocity information, including the full error distribution and its covariances, and the Gaussian that describes the current-day structure of a component in phase-space. We include an assessment of membership probability as part of this analysis. We decide how many components to use to fit a given set of stars by comparing the likelihood of the best fit in each case using the Bayesian Information Criterion (BIC). The BIC is a metric that balances the likelihood against a term that takes into account the number of parameters used to build the model. This term penalizes the BIC (Schwarz 1978) as more parameters are included, which lowers the chance of overfitting the data (see equation 14 and the surrounding text for details). We provide Table 1 as a quick reference for the variables and parameters introduced throughout this section.

---

[1] Here and throughout we adopt a standard XYZ right-handed Cartesian coordinate system where the Sun's position projected on to the Galactic plane lies at the origin in position, the Local Standard of Rest lies at the origin in velocity, and, at the origin, the positive X direction is towards the Galactic centre, the positive Y direction lies in the plane aligned with the direction of Galactic rotation, and the positive Z direction is orthogonal to the Galactic plane. We use $U = \dot{X}$, $V = \dot{Y}$, and $W = \dot{Z}$ to denote velocities in this coordinate system, with $U = V = W = 0$ corresponding to the local standard of rest. As the coordinate system evolves through time it corotates as the origin travels along its circular orbit around the Galaxy, maintaining the axes directions as defined above.

[2] A component is a collection of stars with similar 6D phase-space properties and similar age. A simple association may only require a single component, whereas an association with complex substructure like the Scorpius-Centaurus OB Association might be better described with multiple components.

Table 1. Variables and parameters used in Section 2.

Symbol	Units	Meaning
X, Y, Z	pc	Positional Cartesian dimensions, centred on the Sun's position projected on to the plane of the Galaxy, positive towards Galactic centre, circular rotation, and Galactic North, respectively.
U, V, W	km s^{-1}	Cartesian velocity dimensions, centred on the local standard of rest, with same orientation as X, Y, and Z, respectively.
θ	–	6D phase-space position in *XYZUVW*.
$\mathcal{N}(\theta; \mu, \Sigma)$	–	Evaluation of the 6D Gaussian with mean μ and covariance Σ at the phase-space point θ.
μ_0	–	Modelled centroid of the 6D Gaussian distribution in *XYZUVW* representing the initial kinematic distribution of a component of an association.
t	Myr	Modelled age of a component of an association.
σ_{xyz}	pc	Modelled standard deviation in *X, Y,* and *Z* of initial distribution.
σ_{uvw}	km s^{-1}	Modelled standard deviation in *U, V,* and *W* of initial distribution.
Σ_0	–	Modelled covariance matrix of a 6D Gaussian distribution in *XYZUVW* representing the initial kinematic distribution of a component of an association, constructed from σ_{xyz} and σ_{uvw}.
C	–	A component modelled as a 6D Gaussian in phase-space defined by nine parameters: initial phase-space centroid ($x_0, y_0, z_0, u_0, v_0, w_0$), initial standard deviations in position and velocity space ($\sigma_{xyz}, \sigma_{uvw}$) and time since becoming gravitationally unbound, t.
$p(d\|M)$	–	The likelihood (unscaled probability) of seeing data point d assuming that d was drawn from the modelled distribution M.
$\mathbf{f}(\theta, t)$	–	Abstracted function from `galpy` that numerically integrates the orbit of θ through the Galactic potential as a function of time t.
$\Omega_{i,k}$	–	The overlap integral of the *i*th star with the *k*th component. We calculate this by integrating over the convolution of the two associated 6D Gaussians.
$\mathbf{Z}$	–	2D array of membership probabilities with a row for each star and a column for each component.
w_k	–	Expected fraction of stars belonging to component *k*. We calculate this by summing the *k*th column of $\mathbf{Z}$, and normalizing by the total number of stars.

We begin this section with a top-down description of the algorithm (Fig. 1). We must first decide how many components to use in our fit. A priori we do not know how many components are required to describe an association and so we run the following algorithm iteratively, incrementing the number of components each time, halting when the extra component yields a worse BIC value. For a given component count we use the Expectation Maximization (EM) algorithm (e.g. McLachlan & Peel 2004) to simultaneously find the best parameters of each of the model components as well as the relative membership probabilities of the stars to each component. After initialization of the model parameters, EM iterates through the Expectation step (E-step) and the Maximization step (M-step) until convergence is reached. The E-step consists of calculating membership probabilities to not only each of the components but also to the background field distribution. The M-step utilizes the membership probabilities to find the best parameters for each component through the maximization of an appropriate likelihood function.

We now describe the model bottom up. We begin with the parametrization of a single component's origin as a spherical Gaussian (Section 2.2) and how we evolve this initial distribution to its current-day distribution. Next we summarize the Bayesian approach to computing the likelihood function (Section 2.3) for a single component. Finally we incorporate multiple Gaussian components using the EM algorithm, as well as the background distribution, which is critical for accounting for interlopers.[3]

The basic data on which our method will operate are a set of stars taken from *Gaia* DR2 (Gaia Collaboration 2018). For the purposes of this paper we focus on stars in and around known associations, but in future work the same algorithm can be applied to search for new associations and moving groups. We transform the 6D astrometry of each star into 6D phase-space data *XYZUVW*,

which describes the position and velocity of the star in Galactic coordinates as described in Table 1. In addition to the central values for each star, we have an associated set of measurement errors encapsulated by a covariance matrix. We use the transforms from Johnson & Soderblom (1987) to create a Jacobian from observed astrometry space to Cartesian *XYZUVW* space then use this to transform the covariance matrices (similar to the process detailed in Appendix A). For the spatial coordinate origin we choose a point that coincides with the projection of the Sun on to the Galactic plane (the Sun being 25 pc above it) and whose velocity coordinate origin is given by the local standard of rest (LSR) as given by Schönrich, Binney & Dehnen (2010). For convenience we label this as $\theta_{\mathrm{LSR}} = [0, 0, -25, -11.1, 12.24, -7.25]$ with units as given in Table 1, denoting our coordinate system origin with respect to the Sun. We apply this offset to the data to translate the initially heliocentric data to our chosen coordinate system.

2.2 Modelling a single component

As stated earlier, we use a spherical 6D Gaussian distribution to model the origin of a component. We define the kinematic origin of a collection of stars as the approximation of some precise time and place when the stars become gravitationally unbound. A bound set of stars forms an ellipsoid in both position space and velocity space, with no correlation between the three pairs of position and velocity dimensions ($X - U$, $Y - V$, and $Z - W$). We refer to these three planes as *mixed-phase planes* henceforth. We further simplify matters by approximating the ellipsoid as spherical, thereby removing all correlations between any dimensions. We explore the validity of these assumptions in the discussion.

We parametrize the origin of a component as a Gaussian in 6D phase-space $\theta = [x, y, z, u, v, w]$ with mean μ_0 representing the vector of expectation values in each dimension:

[3]The likelihood function provides a metric on how well a given set of parameter values explains the data.

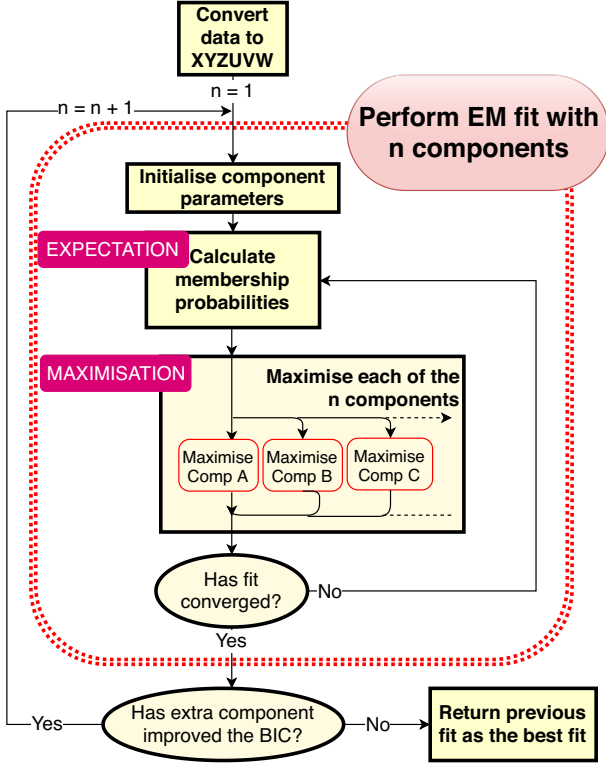$$\mu_0 = [x_0, y_0, z_0, u_0, v_0, w_0]. \tag{1}$$

Figure 1. Layout of the overall fitting algorithm to a set of stellar 6D astrometric data. We first convert the data into Cartesian coordinates *XYZUVW*, centred on the local standard of rest. We then perform an Expectation Maximization (EM) fit (detailed in Section 2.4), initially with the number of components (described in Section 2.2) *n* set to 1, then subsequently incremented until the inclusion of an extra component worsens the fit, as determined by the Bayesian information criterion (BIC). As part of the maximization step, we maximize each component's set of parameters using Markov Chain Monte Carlo sampling, by first constructing a Gaussian distribution in 6D phase-space as defined by the parameters, then projecting it forward through time by the modelled age, before comparing it to its assigned members (see Fig. 2).

To satisfy the criteria stated above we parametrize the covariance matrix Σ_0 as:

$$\Sigma_0 = \begin{bmatrix} \sigma_{xyz}^2 & 0 & 0 & 0 & 0 & 0 \\ 0 & \sigma_{xyz}^2 & 0 & 0 & 0 & 0 \\ 0 & 0 & \sigma_{xyz}^2 & 0 & 0 & 0 \\ 0 & 0 & 0 & \sigma_{uvw}^2 & 0 & 0 \\ 0 & 0 & 0 & 0 & \sigma_{uvw}^2 & 0 \\ 0 & 0 & 0 & 0 & 0 & \sigma_{uvw}^2 \end{bmatrix}. \quad (2)$$

Note that since we restrict our model to be separately spherical in both position and velocity space we can denote the initial standard deviation in each position axis (i.e. the radius of the association) as σ_{xyz} and the initial velocity dispersion in each velocity axis as σ_{uvw}. Hence we can express the probability density associated with each component as a Gaussian distribution over $\boldsymbol{\theta}$:

$$\mathcal{N}(\boldsymbol{\theta}; \boldsymbol{\mu}_0, \boldsymbol{\Sigma}_0) = \frac{\exp\left[-\frac{1}{2}(\boldsymbol{\theta} - \boldsymbol{\mu}_0)^T \boldsymbol{\Sigma}_0^{-1}(\boldsymbol{\theta} - \boldsymbol{\mu}_0)\right]}{\sqrt{(2\pi)^6 |\boldsymbol{\Sigma}_0|}}. \quad (3)$$

In order to relate the distribution of a component to observed stellar data we require the phase-space values of both the component
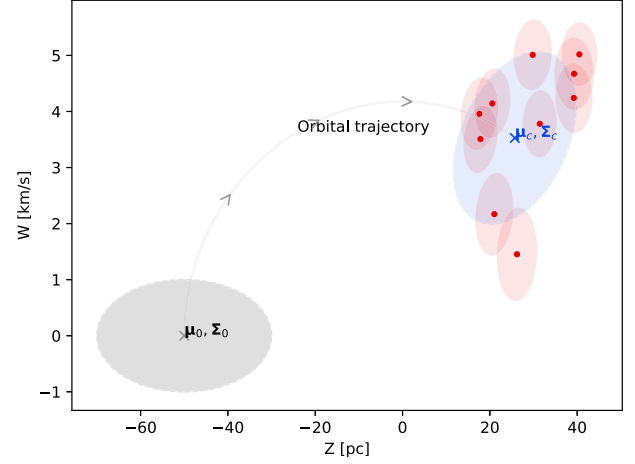

Figure 2. A basic schematic detailing how a single Gaussian component is fitted to stellar data. The red points represent stellar data at current-day (e.g. as measured by *Gaia* DR2) with 2σ uncertainties denoted by ellipses. The grey ellipse and cross depict the modelled initial distribution, a 6D Gaussian with mean $\boldsymbol{\mu}_0$ and covariance matrix $\boldsymbol{\Sigma}_0$. The fitting process projects the initial distribution forward by the component's modelled age which generates the current-day distribution with mean $\boldsymbol{\mu}_c$ and covariance matrix $\boldsymbol{\Sigma}_c$, depicted by the blue ellipse and cross, respectively. The orbital trajectory is denoted by the grey arc, with arrows denoting travel forward through time. For simplicity, we only show the $Z - W$ slice through the 6D phase-space but Chronostar makes use of the full 6D phase-space information.

model and the stellar data to be evaluated at the same time. We transform the distribution of a component from its origin (parametrized by $\boldsymbol{\mu}_0$ and $\boldsymbol{\Sigma}_0$) forward through the Galactic potential by its modelled age *t*, to its current-day distribution, another Gaussian described by $\boldsymbol{\mu}_c$ and $\boldsymbol{\Sigma}_c$, i.e. $\mathcal{N}(\boldsymbol{\theta}; \boldsymbol{\mu}_c, \boldsymbol{\Sigma}_c)$ (see Fig. 2). Using galpy (Bovy 2015) to calculate orbits, we transform the shape of the Gaussian by considering the orbital projection of the distribution as a transformation between coordinate frames. We use galpy's model MWPotential2014 as our model for the Galactic potential, but we show in Appendix B that choosing other plausible potentials does not lead to large differences in the results. We can thus calculate the current-day distribution by performing a first-order Taylor expansion about $\boldsymbol{\mu}_0$, and generating the current-day covariance matrix $\boldsymbol{\Sigma}_c$ under the approximation that this coordinate transformation is linear (details in Appendix A).

2.3 Fitting approach

Now that we have the means to get the current-day distribution of a component from its modelled origin point, we can use a Bayesian approach to generate a probability distribution of the model's parameter space, which will allow us to identify each parameter's most likely value and associated uncertainty. As is standard with a Bayesian approach, we write the posterior probability distribution of the model parameters ($C = \{\boldsymbol{\mu}_0, \boldsymbol{\Sigma}_0, t\}$) given the data as the product of the prior probabilities with the likelihood function:

$$p(C|D) \propto p_{\text{prior}}(C) p(D|C). \quad (4)$$

The prior (p_{prior}) represents our initial guess at the parameters in the absence of data, for example a restriction that the initial spread, dispersion, and approximate mass of the system be super-virial (see Section 2.5 for details). The likelihood function $p(D|C)$ is simply the probability density of the data given the model.

In our context the data D are composed of a set of N stars $\{s_1, s_2, \ldots, s_n\}$ that are candidate members of a component C, each with full 6D kinematic information. From the method described in Section 2.2 we produce a current-day distribution $(\boldsymbol{\mu}_c, \boldsymbol{\Sigma}_c)$ from the model component parameters. We interpret the current-day Gaussian as the probability density of finding a member of C at phase-space position $\boldsymbol{\theta}$. If measurements were infinitely precise this would be $\mathcal{N}(\boldsymbol{\theta}; \boldsymbol{\mu}_c, \boldsymbol{\Sigma}_c)$ and the likelihood function for a set of N stars drawn independently would simply be $p(D|C) \propto \prod_i^N \mathcal{N}(\boldsymbol{\theta}_i; \boldsymbol{\mu}_c, \boldsymbol{\Sigma}_c)$. However, measurements of $\boldsymbol{\theta}_i$ have finite errors, which we take to be Gaussian, described by the probability distribution $\mathcal{N}(\boldsymbol{\theta}; \boldsymbol{\mu}_i, \boldsymbol{\Sigma}_i)$, where $\boldsymbol{\mu}_i$ is the central estimate and $\boldsymbol{\Sigma}_i$ is the covariance of measurement errors. The likelihood product therefore becomes the product of convolutions of the Gaussian for component C with the Gaussians describing the error ellipse for each star:

$$p(D|C) \propto \prod_{i=1}^N \int \mathcal{N}(\boldsymbol{\theta}; \boldsymbol{\mu}_i, \boldsymbol{\Sigma}_i) \mathcal{N}(\boldsymbol{\theta}; \boldsymbol{\mu}_c, \boldsymbol{\Sigma}_c) \, d\boldsymbol{\theta} \equiv \prod_{i=1}^N \Omega_{i,c}, \quad (5)$$

where $\boldsymbol{\mu}_i$ and $\boldsymbol{\Sigma}_i$ are the central estimate and covariance matrix for the ith star, respectively, and

$$\Omega_{i,c} = \frac{\exp\left[-\frac{1}{2} \left(\boldsymbol{\mu}_i - \boldsymbol{\mu}_c \right)^T \boldsymbol{\Sigma}_{i,c}^{-1} \left(\boldsymbol{\mu}_i - \boldsymbol{\mu}_c \right) \right]}{\sqrt{(2\pi)^6 \, |\boldsymbol{\Sigma}_{ic}|}} \quad (6)$$

$$\boldsymbol{\Sigma}_{i,c} = \boldsymbol{\Sigma}_i + \boldsymbol{\Sigma}_c. \quad (7)$$

Equation (6) is the standard result for the convolution of N-dimensional Gaussians; note that in the limit of no errors ($\boldsymbol{\Sigma}_i \to \mathbf{0}$), the result trivially reduces to $\Omega_{i,c} = \mathcal{N}(\boldsymbol{\mu}_i; \boldsymbol{\mu}_c, \boldsymbol{\Sigma}_c)$ as described above. For convenience in what follows, we shall refer to $\Omega_{i,c}$ as the overlap integral of star i with component C.

2.4 Fitting many components with the expectation maximization algorithm

We now describe how to extend our formalization so as to incorporate multiple Gaussian components, i.e. a Gaussian Mixture Model. Our model M is a linear combination of K components $\{C_1, C_2, \ldots, C_k\}$, and has the probability distribution function (PDF):

$$p(\boldsymbol{\theta}|M) = \sum_{k=1}^K w_k \mathcal{N}(\boldsymbol{\theta}; \boldsymbol{\mu}_k, \boldsymbol{\Sigma}_k), \quad (8)$$

where w_k is the weighting of each component such that $\sum_k w_k = 1$. Intuitively w_k is the expected fraction of stellar members belonging to component k. We calculate w_k by summing the kth column of $\mathbf{Z}$ (defined below) and normalizing by the total number of stars.

To simplify the maximization of the likelihood function, the common approach is the Expectation Maximization (EM) algorithm (McLachlan & Peel 2004). There are many derivations of this algorithm, but for convenience we provide a brief summary. The central problem in mixture models is how to assign particular stars to particular components. EM addresses this by introducing a so-called *hidden* variable $\mathbf{Z}$ that tracks each star's membership probabilities. $\mathbf{Z}$ is a matrix of N rows (for each star) and K columns (for each component). Each entry is a decimal number between 0 and 1 such that each row sums exactly to 1. In this way the ikth element of $\mathbf{Z}$ is the probability that the ith star is a member of the kth component.

The expectation step (E-step) and maximization step (M-step) have a circular dependency: one cannot know the membership

probabilities without a fit to the components, and one cannot fit the components without knowing which stars are members. This is solved by, after a carefully chosen initialization (described below), the algorithm alternating between the E-step (evaluating $\mathbf{Z}$) and the M-step (maximizing each component's likelihood function) until convergence is achieved. We can initialize this method by either using membership probabilities from the literature to guess our $\mathbf{Z}$, or by using fits to the distribution from the literature to guess the model parameters for the origin. We defer a more detailed discussion of how we initialize our fits to Section 2.7.

The E-step is the calculation of $\mathbf{Z}$ for a fixed set of components. The relative probability that star i is a member of component k with properties C_k is given by its overlap integral with that component scaled by the component weight w_k, so the total probability that it is a member of component k is

$$Z_{ik} = \frac{w_k \Omega_{i,k}}{\sum_{j=1}^K w_j \Omega_{i,j}}, \quad (9)$$

where we use $\Omega_{i,k}$ to denote the overlap integral (equation 6) evaluated using $\boldsymbol{\mu}_c = \boldsymbol{\mu}_k$ and $\boldsymbol{\Sigma}_c = \boldsymbol{\Sigma}_k$, i.e. using the central location and covariance matrix for component k.

The M-step maximizes the likelihood function for fixed membership probabilities. By the introduction of $\mathbf{Z}$, the likelihood function becomes separable, allowing us to maximize each component's contribution in isolation.

The likelihood function for each component is the same as the likelihood function evaluated for a single component (equation 5), modified so that each star is weighted by the probability that it is a member:

$$p(D|C_k, \mathbf{Z}) \propto \prod_{i=1}^N (w_k \Omega_{i,k})^{Z_{ik}} \quad (10)$$

In the M-step, we use Markov Chain Monte Carlo (MCMC) (implemented by Foreman-Mackey et al. 2013 as emcee) to find the maximum likelihood values of $\boldsymbol{\mu}_k$ and $\boldsymbol{\Sigma}_k$ given the likelihood function $p(D|C_k, \mathbf{Z})$ and the priors we place on C_k (see below). We reset $\boldsymbol{\mu}_k$ and $\boldsymbol{\Sigma}_k$ to these maximum likelihood values and then return to the E-step for another iteration. The algorithm continues in this manner until converged, which we take to be when the previous iteration's best-fitting parameters all fall within the central 70th percentile of the new fit's respective posterior distribution.

2.5 Priors

Our Bayesian treatment of data requires a prior on the parameters t_k, $\boldsymbol{\mu}_{k,0}$, and $\boldsymbol{\Sigma}_{k,0}$ that describe each component. We first discuss our *non-informative* priors. We have a uniform prior on t_k and each element in $\boldsymbol{\mu}_{k,0}$. The covariance matrix $\boldsymbol{\Sigma}_{k,0}$ is parametrized by only two values, σ_{xyz} and σ_{uvw}, both of which are standard deviations. Since standard deviations are by definition restricted to be positive, the natural non-informative prior is uniform in $\ln \sigma$ rather than in σ itself, which corresponds to $p_{\text{prior}}(\sigma) \propto 1/\sigma$. Therefore, our prior on $\boldsymbol{\Sigma}_{k,0}$ is

$$p_{\text{prior}}(\boldsymbol{\Sigma}) \propto p_{\text{prior}}(\sigma_{xyz}) p_{\text{prior}}(\sigma_{uvw}) \propto \frac{1}{\sigma_{xyz}\sigma_{uvw}}. \quad (11)$$

We also add an informative prior regarding the dynamical state of purported origin sites. In testing we found that there is a mild degeneracy shared by the initial spatial volume of an association and its age, whereby some fits would collapse to an extremely small σ_{xyz}. This is unphysical, since such a tightly packed association

would have been gravitationally bound and thus would not have dispersed in the first place. To counter this, we introduce a prior on the virial ratio α of our components, which we approximate as

$$\alpha = \frac{2\sigma_{uvw}^2\sigma_{xyz}}{GM}, \tag{12}$$

where M is the mass of the proposed component and G is the gravitational constant. The mass of the association is not precisely known, since often the masses of individual stars are constrained only poorly, and our lists of candidate members are magnitude-limited and thus likely omit a significant number of low-mass stars. As a very rough estimate we adopt $M = nM_\odot$ for the purpose of computing α, where n is the number of stars in a proposed component. This amounts to assuming solar mass stars. We apply a prior with a Gaussian distribution on the natural logarithm of α with a mean of 2.1 and a standard deviation of $\sigma_\alpha = 1.0$. We select these values such that the mode of the corresponding lognormal distribution occurs at $\alpha = 3$. We find that smaller values of σ_α smoothly increase the fitted age when applied to real data as the fit prioritizes more compact origins regardless of the data, whilst the age fit converges for $\sigma_\alpha \geq 1$.

2.6 Characterizing field stars

For any proposed member of an association there is always a chance that it is not truly a member, but rather an interloper that happens to share similar kinematic properties. We label these stars as *field* stars, and call the PDF of all field stars the *background* distribution. We use the background distribution to consider the probability that a star is a member of the background, and thus properly quantify the star's membership probability to our association fits.

We determine our background distribution, which is held fixed, as follows. We select all *Gaia* DR2 stars with radial velocities and parallax errors better than 20 per cent ($n = 6\,376\,803$ stars), and then transform the data into Galactic Cartesian coordinates (*XYZUVW*) as described in Section 2.1. We estimate the background PDF shape in these coordinates using a Gaussian Kernel Density Estimator (KDE) to approximate a continuous PDF. The KDE we use[4] represents the PDF as a sum of Gaussians centred on each of the n input data points; these Gaussians have a covariance matrix equal to the covariance matrix of the input data set, scaled down by the square of a dimensionless factor called the *bandwidth*. To be precise, we estimate the background stellar density at a point $\boldsymbol{\theta}$ in parameter space as

$$p(\boldsymbol{\theta}) = \sum_i \mathcal{N}(\boldsymbol{\theta}; \boldsymbol{\mu}_i, h^2\boldsymbol{\Sigma}_G), \tag{13}$$

using notation from equation (3), where the sum runs over the n stars in the *Gaia* DR2 catalogue with acceptably small errors, $\boldsymbol{\Sigma}_G$ is the covariance matrix of this catalogue, $\boldsymbol{\mu}_i$ is the *XYZUVW* position of star i, and h is the bandwidth. We determine h using Scott's Rule (Scott 1992):

$$h = n^{-1/(d+4)},$$

where $d = 6$ is the number of dimensions, resulting in a bandwidth of ≈ 0.2.

We treat the background as simply another component in our multicomponent fits, i.e. in a fit with K components, the parameter $\mathbf{Z}$ is an $N \times (K + 1)$ matrix, with the final column $K + 1$ giving

---

[4]`scipy.stats.Gaussian_kde` (Jones et al. 2001)

the probability that a given star is a background star rather than a member. Our treatment of the background differs from that of other components only in that the background is static and does not have any parameters that can change, so the overlap integral between it and each star $\Omega_{i,K+1}$, is a constant that may be computed once at the beginning of our calculation and then stored for use when needed. We further note that the background is essentially constant over scales in *XYZ* and *UVW* comparable to the sizes of measurement uncertainties, and thus we can approximate the overlap integrals $\Omega_{i,K+1}$ as simply the value of the background evaluated at the central position and velocity estimates for each star.

2.7 Initialization and adding components

Each run of `Chronostar` begins with a single component, which is described by nine scalar quantities: the six components of the central phase-space position $\boldsymbol{\mu}_0$, the initial spatial, and velocity dispersions σ_{xyz} and σ_{uvw}, and the age t. We initialize an MCMC search for the maximum likelihood in the 9D space these parameters describe by placing walkers randomly around a central starting guess, which is that the components of $\boldsymbol{\mu}_0$ are equal to the mean of the stellar data to which we are fitting, $\sigma_{xyz} = 20$ pc, $\sigma_{uvw} = 7\,\mathrm{km\,s^{-1}}$, and $t = 3$ Myr. We then run the MCMC algorithm to maximize the likelihood function as described in Section 2.4, stopping when we reach convergence. At this point we have predicted posterior probability distributions for all nine quantities.

To trial an alternative two-component fit, we must specify a starting guess for the parameters of each of the two components, which will serve as starting points about which to distribute initial MCMC walker positions. We choose these starting guesses as follows. For each proposed component, we take our starting guesses for σ_{xyz} and σ_{uvw} to be equal to the maximum posterior probability value derived from the one-component fit. We set the starting time guesses for our two proposed components equal to the 16th and 84th percentile values of the posterior probability distribution for t from the one-component fit. Finally, we set our starting guess for the phase-space position $\boldsymbol{\mu}_0$ of each of the two trial components such that their *current-day* positions match the *current-day* centroid position of the maximum posterior probability value for the one-component fit. From these starting guesses, we run the EM algorithm as described in Section 2.4, stopping when we converge. We then compute the BIC for the one-component versus the two-component fit using the following formula:

$$\mathrm{BIC} = \ln(n)k - 2\ln\mathcal{L}, \tag{14}$$

where n is the expected number of stars assigned to the components, k is the number of parameters, and $\mathcal{L}$ is the evaluated likelihood. If the two-component BIC is inferior to the one-component result, we stop and accept the one-component result. If not, we accept the two-component fit, and consider the possibility of adding a third component.

The procedure for going beyond two components is much the same as for going from one to two: we initialize a search by splitting an existing component into its 16th and 84th percentile ages, setting our central guesses for the initial phase-space positions and dispersions exactly as we did when going from one to two components. The primary complication is that there is no obvious means to identify which existing component should be split in order to yield the best fit. Thus `Chronostar` explores all possible splits, carries out EM to find the posterior probability for each possibility, then selects the best option between these and the previous fit to one

fewer components based on the BIC. We stop adding components when the fit with N components has a superior BIC compared to any of the possible fits using $N + 1$ components.

We caution that this procedure does not necessarily guarantee the identification of the best possible fit, especially when the number of components is relatively large. As is usual with MCMC over high-dimensional spaces (a fit to N components has $9N$ dimensions), there is in general no way to guarantee that the true global maximum likelihood has been found. However, Section 3.3 demonstrates that even this basic approach successfully decomposes complex associations with multiple components.

The time taken to complete a fit is strongly dependent on the number of components required, but also depends on the number of stars and the age of the components. Each EM iteration takes an average 500–1000 MCMC steps per component. The number of EM iterations needed for convergence can vary from about 30 iterations (in the case where there is a clear sub-component needing characterization) to upwards of 150 iterations (where the introduced component has not identified a separate distinct overdensity). Simple arrangements, such as the multicomponent tests we present in the next section, require only ∼10 h for convergence running on a workstation or a single node of a cluster. A blind fit to ∼2000 stars will take upwards of a week on the same hardware. In the case of our βPMG fit (see Section 4), we ran the fit with 19 threads (1 per each of the 18 walkers plus one master thread)[5] and the computation took about a week to converge. Due to these limitations, if Chronostar were to be fit to all of *Gaia*, the data would need to be parcelled into subsets of a few thousand stars at a time.

3 TESTING CHRONOSTAR WITH SYNTHETIC DATA

We investigate the reliability and accuracy of our fitting approach by testing it on an extensive suite of 1080 synthetic single-component associations, three scenarios with multiple components, a set of stellar kinematics taken from a star formation simulation (Federrath 2015; Federrath, Krumholz & Hopkins 2017), and a two-component association within a uniform background. We describe each of these tests in turn in the following sections.

3.1 Single-component analysis

Our first test is the simplest, and uses as its mock data single components constructed from the same distributions we have assumed can be used to describe real associations. Thus we consider origin sites that are spherical in both position and velocity space, and are parametrized by five values: age t (i.e. how many years have passed since becoming unbound), σ_{xyz}, the standard deviation in each position dimension, σ_{uvw}, the velocity dispersion or standard deviation in each velocity dimension, n, the number of stars drawn from the distribution, and η, which characterizes the uncertainty of the observed current-day properties as described below. The purpose of this test is to ensure that our code can recover input data whose properties match our assumptions, and to characterize the level of accuracy we can expect in this optimal case.

We use our chosen parameters to construct a synthetic data set in several steps, which we explain in more detail below: (1) we

use t, σ_{xyz}, and σ_{uvw} to compute the starting centroid position μ_0 and covariance matrix Σ_0 for our synthetic association; (2) we use μ_0 and Σ_0 plus the specified number of stars n to create a set of synthetic initial positions and velocities, which we then integrate forward by time t to produce a set of synthetic current-day positions and velocities; (3) we add synthetic errors, whose sizes are parametrized by η, to yield a set of 'observed' stars on which we run the Chronostar code.

Step (1) is to compute μ_0 and Σ_0. For the latter we set $\Sigma_{00} = \Sigma_{11} = \Sigma_{22} = \sigma_{xyz}^2$ and $\Sigma_{33} = \Sigma_{44} = \Sigma_{55} = \sigma_{uvw}^2$, following the assumption that our initial conditions are spherical distributions; all off-diagonal components of Σ_0 are zero. For the former, we choose a starting position so that the current-day centroid position of our synthetic association matches that of Lower Centaurus-Crux (LCC), $\mu_{LCC} = [50, -100, 25, 1.1, 7.76, 2.25]$ (see Table 1 for units) by integrating an orbit backwards through time for the desired age t, beginning at the desired current-day centroid μ_c. In other words: $\mathbf{f}(\mu_0, t) = \mu_{LCC}$, where $\mathbf{f}(\mu_0, t)$ is the function that maps an initial position μ_0 to a final position μ after orbiting a time t through the Galactic potential. This choice ensures the synthetic associations are all at the same heliocentric radius, thus preserving consistency with measurement uncertainties that are distance dependent.

Step (2) is drawing n stars from a 6D Gaussian distribution with centroid μ_0 and covariance matrix Σ_0. We then integrate these stars forward through the Galactic potential for a time t. We convert the current-day position of each star from Cartesian Galactic coordinates to astrometric coordinates (RA, DEC, μ_{RA}, μ_{DEC}, parallax, and radial velocity).

Step (3) is to add synthetic errors. We use the median uncertainties of *Gaia* DR2 to inform our artificial measurement uncertainties. Of all the *Gaia* DR2 stars with radial velocities and parallax uncertainty better than 20 per cent, the median uncertainties for parallax, proper motion, and radial velocity are 0.035 mas, 0.05 mas yr^{-1} and 1 km s^{-1}, respectively. We set the uncertainties on our synthetic data by multiplying these values by a dimensionless scale factor η, so that the parallax uncertainty is 0.035η mas, the proper motion uncertainty is 0.05η mas yr^{-1}, and the radial velocity uncertainty is 1η km s^{-1}. For each synthetic star, we add a random offset to its astrometric coordinates chosen by drawing from a Gaussian distribution of the specified size.

We generate 1080 synthetic associations by creating four realizations for each possible combination of the parameters:

$$\text{age, } t = [5, 15, 30, 50, 100]\,\text{Myr,}$$

$$\text{radius, } \sigma_{xyz} = [1, 2, 5]\,\text{pc,}$$

$$\text{velocity dispersion, } \sigma_{uvw} = [1, 2]\,\text{km s}^{-1},$$

$$\text{star count, } n = [25, 50, 100],$$

$$\text{error scaling, } \eta = [0.5, 1, 2].$$

We choose this range of parameters to be broadly representative of known or claimed moving group origin sites. However, the maximum values of σ_{uvw} and t for which we test deserve special mention, because they are driven in part by the limitations of our method. In deriving the likelihood function we have approximated the time evolution of the PDF of phase-space density with a linear transformation, and we show below that this approximation breaks down for association ages ≫100 Myr, or velocity dispersions ≫2 km s^{-1}.

For each synthetic association we run Chronostar using a single component; the output of the run is a set of MCMC walker positions in the space $(t, \mu_0, \sigma_{xyz}, \sigma_{uvw})$. From these positions, we

---

[5]Each component could, in principle, be fitted concurrently in the maximization stage. However, we have thus far not implemented parallelism in this step, so each component is maximized sequentially.
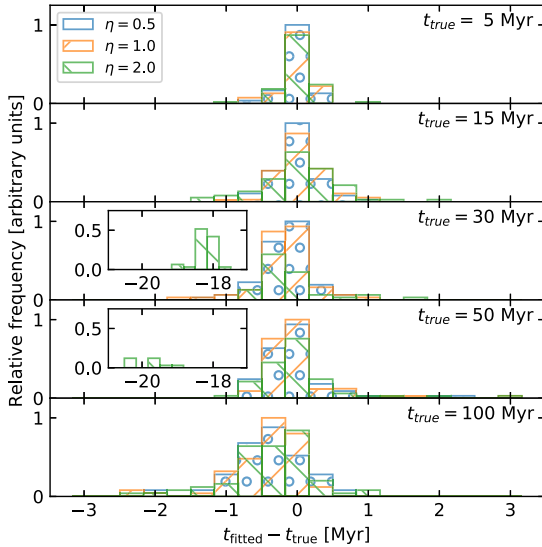
Figure 3. Histograms of residuals $t_{fitted} - t_{true}$ resulting from application of Chronostar to 1080 synthetic associations, grouped by true age (panels, increasing from top to bottom) and degree of measurement uncertainty (histograms in each panel). The catastrophic failures (featured in the insets) all cluster around 20 Myr, which is equal to the quarter period of vertical oscillations through the Galactic plane.
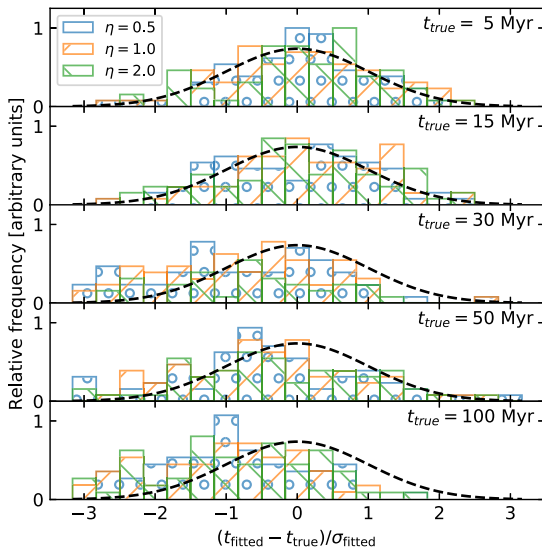

Figure 4. Same as Fig. 3, except that we show the distribution of normalized residuals $(t_{fitted} - t_{true})/\sigma_{fitted}$ rather than the distribution of raw residuals. For comparison, the black lines in each panel show Gaussian distributions with zero mean and unit variance, scaled such that the area under the curve matches the area under the $\eta = 0.5$ histogram in each panel, and thus shows the distribution of normalized residuals we would expect if the true posterior PDF were Gaussian. We do not include the catastrophic failures in this figure.

define t_{fitted} as the median t coordinate of the walkers, and the corresponding fit uncertainty σ_{fitted} as half the difference between the 16th and 84th percentiles of t.

Fig. 3 shows the distribution of raw residuals, $t_{fitted} - t_{true}$ (where t_{true} is the true age used to generate the synthetic data set) that we obtain from our experiment, and Fig. 4 shows the corresponding normalized residuals, $(t_{fitted} - t_{true})/\sigma_{fitted}$; in both cases the data are grouped by values of t_{true} and η. The raw residuals characterize

the absolute accuracy of the method, while the distribution of normalized residuals characterize the accuracy of the error estimate it returns.

We find that, except for a small number of catastrophic failures that are easy to spot and discussed below, Chronostar recovers the correct ages to accuracies of ~ 1 Myr almost independent of t_{true} or η. There is a systematic bias towards younger ages that increases with t_{true}, reaching a maximum net offset of ~ 0.3 Myr at $t_{true} = 100$ Myr. We attribute this offset to the associations' minor yet potential departures from the linear regime. The normalized residuals show distributions that are close to Gaussians with unit dispersion, indicating that the error distribution for our method is close to Gaussian, and that the returned σ_{fitted} is an accurate estimate of the true uncertainty. Again we see a slight bias towards younger ages that worsens for older t_{true}.

It may seem surprising that the age fits have an uncertainty so robust to t_{true}. However ultimately the uncertainty of the age fit depends on how accurately Chronostar fits the correlation in the three mixed phase-space planes ($X - U$, $Y - V$, and $Z - W$), as these are the signatures of expansion. The stars mostly remain in the linear regime so these correlations are linear regardless of the age, therefore the reliability of the age fit is almost independent of age.

Fig. 3 shows that our method catastrophically fails for a small number of cases where the true age is 30 or 50 Myr, and the error normalization is $\eta = 2$ (i.e. double the fiducial errors of *Gaia* measurements). In these cases, the fitted ages consistently fall short by about 20 Myr. This is a consequence of a degeneracy in the $Z - W$ plane. The matter density in the Galaxy is reasonably constant with ≈ 100 pc of the Galactic plane (formally, for our standard model of the Galactic potential, the density at 100 pc is 85 per cent of the mid-plane density), making the vertical restoring force close to linear in a star's distance from the mid-plane, and thus similar to that of a simple harmonic oscillator. Consequently, each star in our synthetic associations has nearly the same period in the Z direction, and thus for a particular current-day distribution of stellar positions and velocities there is a degeneracy between two possible starting states: stars could have started at similar heights but a wide range of velocities, or with a small range of velocities but a large variation in starting heights. The phase-space distribution of the stellar population in the $Z - W$ plane is therefore uncorrelated at multiple distinct epochs, separated by a quarter of the vertical oscillation period, which is ≈ 20 Myr. Our catastrophic failure mode consists of the MCMC walkers settling into the first of these many degenerate minima that yields a reasonable fit in other phase-space dimensions. This failure mode only occurs for errors larger than usual for *Gaia*, because for smaller errors, constraints in the phase-space components that lie in the Galactic plane are sufficient to break the degeneracy in the out-of-plane directions. Thus, these failures are not a concern for practical applications, as long as the relative uncertainties for the majority of stars in question do not significantly exceed 100 per cent that of *Gaia*.

3.2 Stars with realistic initial kinematics

In the previous section, all our synthetic associations had initial conditions that matched our assumptions (spherical, uncorrelated initial distribution; instantaneous gravitational unbinding). Here we consider a much more realistic initial stellar distribution by using stellar positions and velocities drawn from a simulation of star formation. The simulation we use is the run referred to as case 'GTBJR' in Onus, Krumholz & Federrath (2018); its initial conditions and physics are identical to the 'GvsTMJ' case presented

in Federrath (2015), which includes turbulence, magnetic fields, and jet feedback, but with the addition of radiation feedback as implemented in Federrath et al. (2017). The simulation tracks the collapse of a molecular cloud in a 2 pc cube with periodic boundaries. In the simulation, stars are represented by sink particles, and for this test we take the positions and velocities of the sink particles in the final snapshot of the simulation as the initial positions and velocities of synthetic stars. As in the previous tests, we choose the absolute position and velocity of the stars in Galactic coordinates such that their current-day central position and velocity match that of LCC. We project the stars forward through time for 20 Myr, ignoring any gravitational interactions between them, convert their positions and velocities to astrometric coordinates, and add random errors with a distribution equal to our fiducial *Gaia* DR2 median uncertainty ($\eta = 1$; see Section 3.1). We then run Chronostar on the resulting synthetic data set.

Chronostar retrieves an age of 20.1 ± 0.2 Myr, demonstrating that, in this instance, approximating the initial kinematic distribution of the association as spherically Gaussian is a sufficiently accurate approximation. Fig. 5 shows the current and starting positions of the stars, along with the fit, in four different 2D projections ($X - Y$, $X - U$, $Y - V$ and $Z - W$). We see that the current-day fit provides a good match to the current-day position and velocity, and the corresponding fit to the origin falls within 3 pc of the true average initial position of the stars. One particularly noteworthy feature of this plot is that the correct fit is recovered despite the fact that, due to the relatively large uncertainties in the current-day kinematic properties of the stars, an attempt to trace the stars back in time by integrating their orbits does not show any significant amount of convergence. Thus attempts to reconstruct these stars' origin point by looking for a minimum volume or similar, the approach used in traceback methods, would be unlikely to succeed.

We also note that the reconstruction strongly favours a single-component fit to this data set. Following the procedure outlined above, after finding a single component fit, Chronostar attempted a two-component fit. However, the BIC of the single-component fit, 546.5, is significantly better than that of the best two-component fit, 576.5.

3.3 Multiple components

Our next tests increase the complexity by introducing data sets with multiple components, arranged so that they have significant overlap in position, velocity, or both with incorporated observational uncertainties equal to our fiducial *Gaia* DR2 median uncertainty ($\eta = 1$). The goal is to test Chronostar's ability to separate such overlapping sets of stars. We initialize each fit in the default way as described in Section 2.4.

In the following text, for convenience we will refer to stars being *assigned* to components. We remind the reader that Chronostar does not assign discrete memberships but rather utilizes continuous, probabilistic memberships. However, for convenience of plotting and discussion we will describe a star as being assigned to the component for which Chronostar gives the highest membership probability.

3.3.1 Four distinct components

The first test features four components, each containing 30–80 stars, that have distinct ages from 3 to 13 Myr yet have current-day distributions that overlap when viewed solely in position space or

solely in velocity space. However, because these components have different ages, they are separable in joint position-velocity space (e.g. in the $Z - W$ plane). We give the full set of initial parameters for each component, and the best fits to them that Chronostar retrieves, in Table 2. We also show the current-day positions of the stars, and Chronostar's fits to them, in two 2D projections of 6D phase-space in Fig. 6.

Chronostar successfully fits the ages, initial positions, and dispersions of each component, and correctly classifies the memberships of all 200 stars, despite the fact that the four components overlap in multiple dimensions. The reason it is able to accomplish this separation becomes clear if we examine panel (b) of Fig. 6, which shows the distribution of stars, and our fits to them, in the $Z - W$ plane. Consider the ellipses in (b) in order of ascending age (C, D, B, A): the angle that the semimajor axes of each component makes with the vertical increases systematically with age. In the $Z - W$ plane these angles rotate with time, completing a full rotation after 80 Myr. Similar rotation occurs with time in the $X - U$ and $Y - V$ planes (not shown), but with a different period. Chronostar is able to separate four components, despite their overlap in both position and velocity, because position–velocity correlations provide a sensitive measure of age since expansion.

3.3.2 Two components with shared trajectory

The second test uses two components with distinct ages of 7 and 10 Myr, but with origin points carefully selected such that the centroids of their current-day distributions are identical. This gives each association an identical orbital trajectory, which results in two distributions that overlap in every possible 2D projection of the 6D phase-space. This scenario presents a challenge to our fitting approach as there is no separation between the components along any dimension. The only distinction between the two components is the *tilt* or degree of correlation in the *mixed-phase* (i.e. position-velocity) planes. We give the full parameters of the two components used in this test, and the fits to them derived by Chronostar, in Table 3, and we show two projections of phase-space in Fig. 7. Chronostar recovers the ages of both of our overlapping components within a 0.2 Myr uncertainty. Only six stars (blue triangles in Fig. 7) of 120 are misclassified, corresponding to a success rate of 95 per cent, which is consistent with the mean membership probability that Chronostar estimates for all stars to their correct component: 94.3 per cent. Thus Chronostar not only returns the correct assignment for the great majority of stars, it provides an accurate estimate of the confidence level of the assignments as well.

3.3.3 Two components against a uniform background

The third test uses two components with distinct ages of 12 and 25 Myr and star counts of 50 and 40, along with a top-hat PDF background with density $10^{-7} \, (\mathrm{pc \, km \, s^{-1}})^{-3}$, chosen to be representative of the density of *Gaia* DR2 stars in the vicinity of βPMG (see Section 2.6 for details). We refer to the two Gaussian components as an association, and to the third component as the background. We set the bounds of the top-hat PDF representing the background to be twice the extent of the association in each dimension, and centre it on the mid-range of the association stars. The resulting bounds of the top-hat
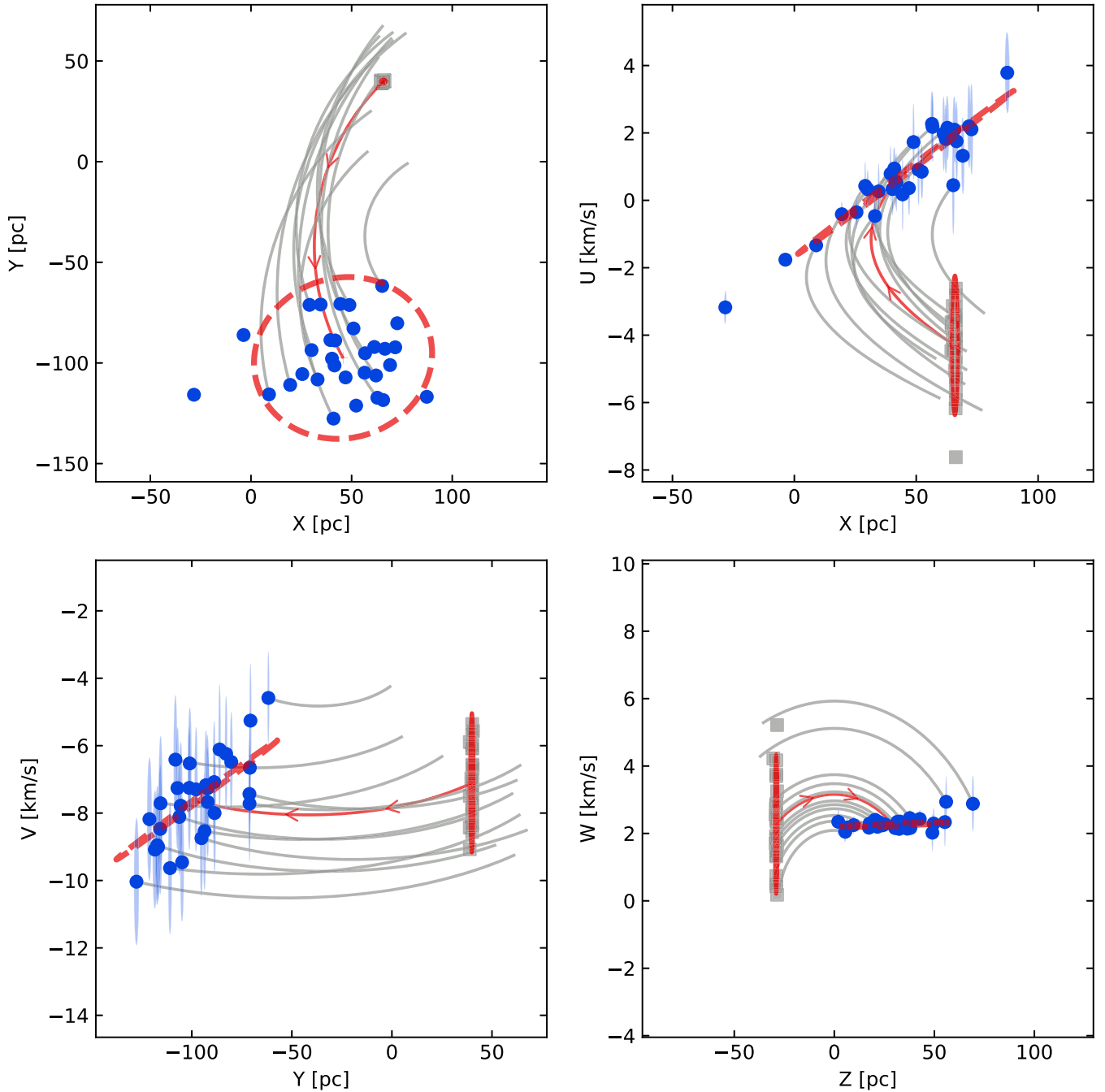
Figure 5. Results from our test using synthetic stars drawn from a star formation simulation (Federrath 2015; Federrath et al. 2017). Panels show the positions of stars at formation 20 Myr ago (grey squares) and at the current-day (blue circles) in several different 2D projections of the 6D phase-space. Faint ellipses around the current-day positions show the error distributions for the synthetic measurement. The dashed red ellipse shows the best-fitting current-day distribution retrieved by Chronostar; a similar best-fitting ellipse for the origin point is also plotted in solid red. The red lines show the trajectory of the centre of the distribution, with arrows pointing forwards through time. The grey lines show the trajectories for selected current-day stars *traced back* from that star's central estimate by 20 Myr. Note that, due to the relatively large uncertainties, these trajectories show minimal convergence in $X - U$ and $Y - V$ planes despite being traced back to their true seeded age. This is not the case for the trajectories in the $Z - W$ plane, which do indeed show convergence in Z. This is a consequence of the almost linear restoring force in the Z direction, resulting in stars having similar periods. See Section 3.1 for further discussion. We note that our choice of a co-rotating reference frame introduces added motion in the X and Y dimensions due to the Coriolis force. As a consequence orbits in the $X - U$ plane curve towards larger values of X despite having U values around $-2\,\mathrm{km\,s^{-1}}$.

Table 2. Parameters for our test using four distinct components with distinct ages but overlapping current-day positions. For each parameter, the 'True' value is the input value used to construct the synthetic data, while the 'Fit' value is the 50th percentile value for the posterior PDF returned by `Chronostar`, with error bars indicating the ranges from the 16th to 50th and 50th to 84th percentiles. The quantity we report for the 'Fit' value of number of stars (nstars) is the sum of the membership probabilities for that component in the final, converged output of the EM algorithm.

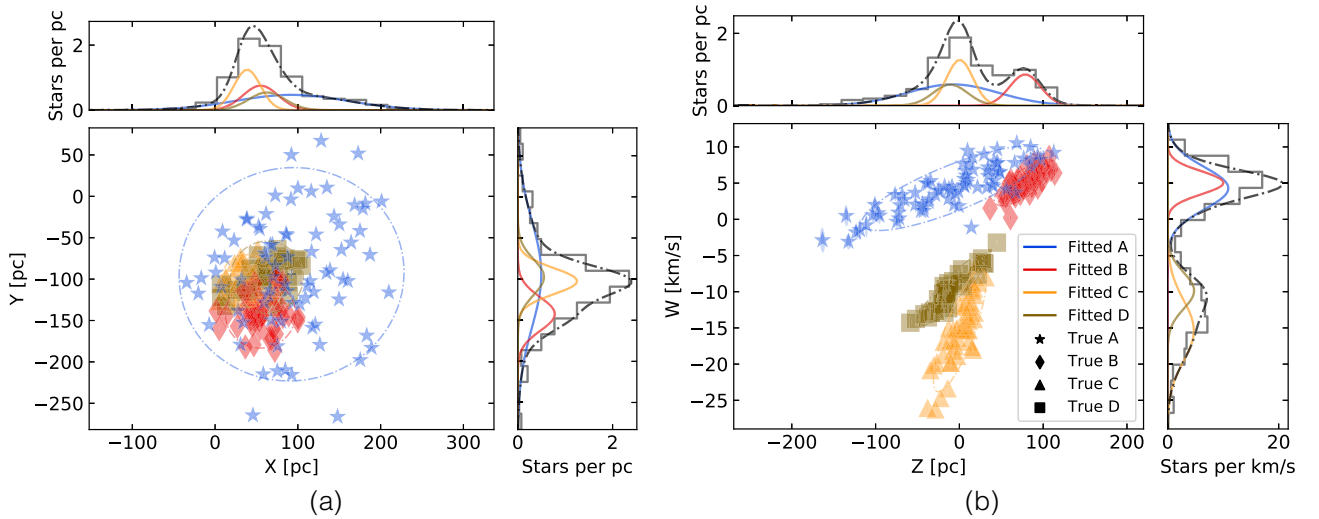|	Component A		Component B		Component C		Component D	
	True	Fit	True	Fit	True	Fit	True	Fit
x_0 (pc)	274.8	$267.2^{+7.2}_{-6.8}$	132.8	$120.7^{+7.0}_{-6.4}$	98.0	$99.9^{+3.8}_{-4.1}$	125.5	$123.8^{+3.3}_{-3.1}$
y_0 (pc)	220.4	$216.7^{+5.2}_{-5.3}$	85.0	$62.2^{+9.9}_{-9.9}$	-46.8	$-48.0^{+3.0}_{-3.1}$	-52.2	$-54.3^{+1.9}_{-2.0}$
z_0 (pc)	-55.6	$-51.6^{+2.4}_{-2.4}$	11.4	$18.0^{+3.9}_{-4.1}$	45.6	$48.3^{+3.0}_{-2.9}$	59.6	$57.7^{+2.6}_{-2.7}$
u_0 (km s^{-1})	-17.3	$-17.4^{+0.6}_{-0.6}$	-12.5	$-11.5^{+0.5}_{-0.5}$	-21.8	$-22.7^{+0.6}_{-0.6}$	-12.4	$-11.8^{+0.6}_{-0.6}$
v_0 (km s^{-1})	-25.1	$-25.1^{+0.6}_{-0.6}$	-22.7	$-23.3^{+0.4}_{-0.4}$	-18.4	$-18.6^{+0.6}_{-0.6}$	-8.2	$-7.6^{+0.6}_{-0.6}$
w_0 (km s^{-1})	2.6	$1.8^{+0.5}_{-0.6}$	7.8	$7.6^{+0.3}_{-0.3}$	-14.6	$-15.0^{+0.6}_{-0.6}$	-9.0	$-8.9^{+0.6}_{-0.6}$
σ_{xyz} (pc)	20.0	$19.4^{+1.0}_{-1.0}$	10.0	$9.6^{+0.8}_{-0.7}$	10.0	$9.4^{+0.6}_{-0.5}$	7.0	$7.8^{+0.7}_{-0.6}$
σ_{uvw} (km s^{-1})	5.0	$4.9^{+0.2}_{-0.2}$	2.0	$2.0^{+0.1}_{-0.1}$	5.0	$4.4^{+0.3}_{-0.2}$	3.0	$3.0^{+0.3}_{-0.2}$
Age (Myr)	13.0	$12.7^{+0.3}_{-0.3}$	10.0	$9.0^{+0.5}_{-0.5}$	3.0	$3.0^{+0.2}_{-0.2}$	7.0	$6.9^{+0.3}_{-0.3}$
nstars	80	80.00	40	40.00	50	50.00	30	30.00

Figure 6. Results from our test using four distinct components with distinct ages but overlapping current-day positions. Panels show the positions of stars at current-day in several different 2D projections of the 6D phase-space. Faint ellipses around the current-day positions show the error distributions for the synthetic measurement but are often smaller than the data points. The dashed ellipses show the best-fitting current-day distributions retrieved by `Chronostar` for each component; see Table 2 for the numerical values of the true and fitted parameters of each component. Marker styles show the component to which each star truly belongs, while marker colours show the component to which `Chronostar` assigns that star; colours and symbols match in all cases because in this test `Chronostar` assigns all stars correctly. Flanking plots show the 1D projection of densities in each dimension. In these plots, histograms show the distribution of synthetic stars, while curves show the probability densities for `Chronostar`'s best fit, and colour indicating component. The grey histogram and black line show the sum of all components.

PDF are:

$$X = (-61.4, 197.6)\,\text{pc},$$

$$Y = (-205.5, 12.6)\,\text{pc},$$

$$Z = (-58.1, 56.8)\,\text{pc},$$

$$U = (-16.5, -4.8)\,\text{km s}^{-1},$$

$$V = (-25.4, -13.9)\,\text{km s}^{-1},$$

$$W = (-9.9, -0.5)\,\text{km s}^{-1}.$$

We draw the true kinematics of 810 stars from this distribution as this achieves the desired overall density. It is straightforward for `Chronostar` to identify the association as it is a prominent

overdensity in both position and velocity space. The challenge lies in how `Chronostar` handles the membership boundaries of an association against a ubiquitous, fixed background distribution.

We give the full parameters of the two components of the association used in this test, and the fits to them derived by `Chronostar`, in Table 4, and we show two projections of phase-space in Fig. 8. `Chronostar` satisfactorily deduces memberships, with only 3 (of 810) background stars misclassified as being part of the association, and only 5 (of 90) association stars misclassified as part of the background. Thus the success rate is 91.4 per cent.[6]

---

[6]Since the boundary of the uniform background stellar distribution is arbitrary, and thus the number of background stars is arbitrary, we disregard correctly assigned background stars when calculating success rates.

Table 3. Parameters for our test using two components with distinct ages but with identical current-day centroids in both position and velocity. See caption to Table 2 for an explanation of the meaning of various table entries.

	Component A		Component B	
	True	Fit	True	Fit
x_0 (pc)	179.7	$179.4^{+2.6}_{-2.7}$	129.5	$128.0^{+2.3}_{-2.3}$
y_0 (pc)	59.1	$57.7^{+0.9}_{-0.9}$	19.5	$16.0^{+2.2}_{-2.1}$
z_0 (pc)	46.1	$46.2^{+0.6}_{-0.5}$	34.1	$31.8^{+1.2}_{-1.3}$
u_0 (km s^{-1})	-16.2	$-15.8^{+0.9}_{-0.9}$	-14.3	$-14.2^{+0.5}_{-0.5}$
v_0 (km s^{-1})	-16.4	$-17.6^{+0.9}_{-0.9}$	-17.8	$-17.6^{+0.5}_{-0.5}$
w_0 (km s^{-1})	-3.6	$-4.5^{+0.9}_{-0.9}$	-4.3	$-4.6^{+0.5}_{-0.5}$
σ_{xyz} (pc)	2.0	$1.9^{+0.3}_{-0.2}$	10.0	$10.3^{+0.5}_{-0.5}$
σ_{uvw} (km s^{-1})	5.0	$4.4^{+0.4}_{-0.3}$	5.0	$4.9^{+0.2}_{-0.2}$
Age (Myr)	10.0	$9.9^{+0.1}_{-0.1}$	7.0	$6.8^{+0.1}_{-0.1}$
nstars	20	23.90	100	96.10

Table 4. Parameters for our test using two components and a uniform background. See caption to Table 2 for an explanation of the meaning of various table entries.

	Component A		Component B	
	True	Fit	True	Fit
x_0 (pc)	546.5	$606.2^{+55.5}_{-58.1}$	269.1	$278.3^{+24.4}_{-22.8}$
y_0 (pc)	91.5	$69.2^{+21.9}_{-26.8}$	63.4	$64.8^{+8.1}_{-9.1}$
z_0 (pc)	58.7	$50.9^{+5.4}_{-5.9}$	51.8	$52.6^{+3.1}_{-3.3}$
u_0 (km s^{-1})	-26.2	$-27.5^{+1.4}_{-1.4}$	-18.1	$-18.7^{+0.8}_{-0.8}$
v_0 (km s^{-1})	-6.2	$-4.4^{+1.6}_{-1.7}$	-15.3	$-15.1^{+0.7}_{-0.6}$
w_0 (km s^{-1})	2.1	$2.8^{+0.6}_{-0.7}$	-2.9	$-2.7^{+0.4}_{-0.4}$
σ_{xyz} (pc)	10.0	$10.2^{+1.0}_{-0.8}$	10.0	$9.3^{+0.7}_{-0.6}$
σ_{uvw} (km s^{-1})	0.7	$0.7^{+0.1}_{-0.0}$	1.0	$1.0^{+0.1}_{-0.1}$
Age (Myr)	25.0	$27.0^{+1.8}_{-2.0}$	12.0	$12.5^{+1.1}_{-1.1}$
nstars	40	38.22	50	46.86

This is similar to the mean membership probability returned by `Chronostar` of all component stars to their true component of origin: 89.2 per cent. If we include the membership probabilities of the misclassified background stars to the background, the mean membership probability is 86.6 per cent. In either case, we see both that `Chronostar`'s membership assignments are reasonably accurate, and, as importantly, that the level of confidence it returns in those assignments is accurate as well.

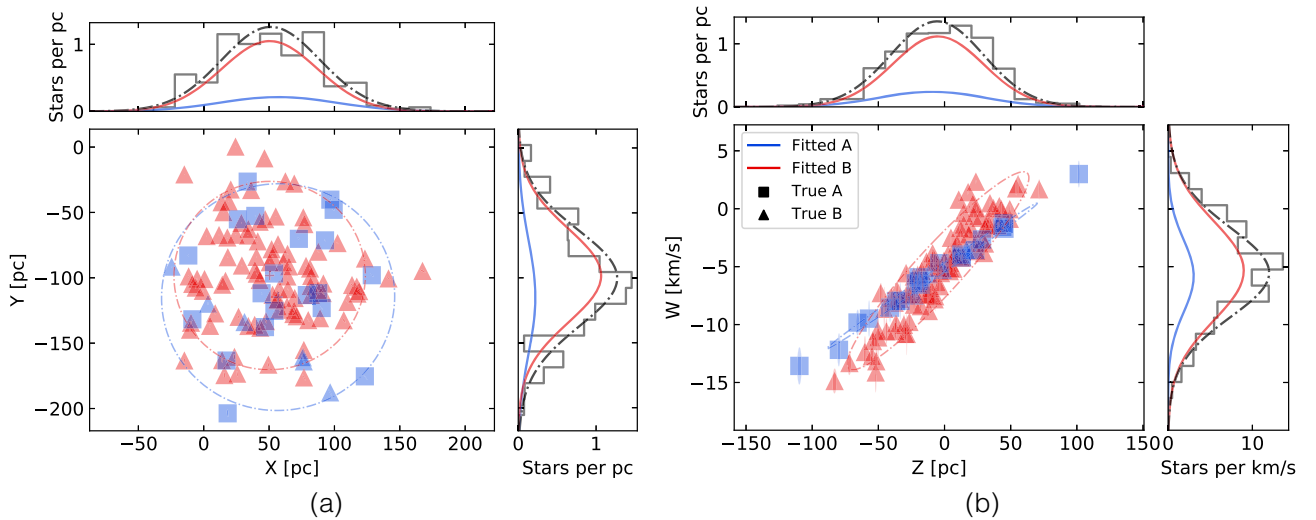## 4 FITTING TO THE β PICTORIS MOVING GROUP

In this section we present the results of `Chronostar` blindly applied to stars in and around the βPMG. The goal is to recover the majority of βPMG members, along with a viable kinematic age, without any manual intervention.

4.1 Input data

The first step in our analysis is to prepare a list of stars on which to run `Chronostar`. We start with the list of βPMG members derived by the BANYAN software package provided by Gagné et al. (2018c), most of which are provided with proper motions and radial velocities compiled from the literature (see Table 7 for details). We cross-match each star in this list with the *Gaia* DR2 catalogue to obtain parallax distances along with improved proper motions and radial velocities where available. In cases where a given piece of kinematic information is available from multiple sources, we use the measurement with the lowest reported uncertainty. We convert all astrometric measurements to *XYZUVW* coordinates as described in Section 2.1. We then remove stars that lack full 6D phase-space information. The result is a set of previously identified βPMG members with full 6D phase space information, including uncertainties. We note that stars without full 6D phase-space information can be included by replacing their

Figure 7. Results from our test using two components with distinct ages but with identical current-day centroids in both position and velocity. See caption to Fig. 6 for an explanation of figure details. Note that six stars (blue triangles) are misclassified corresponding to a success rate of 95 per cent, which is consistent with the mean membership probability that `Chronostar` estimates for all stars with respect to their correct component: 94.3 per cent.
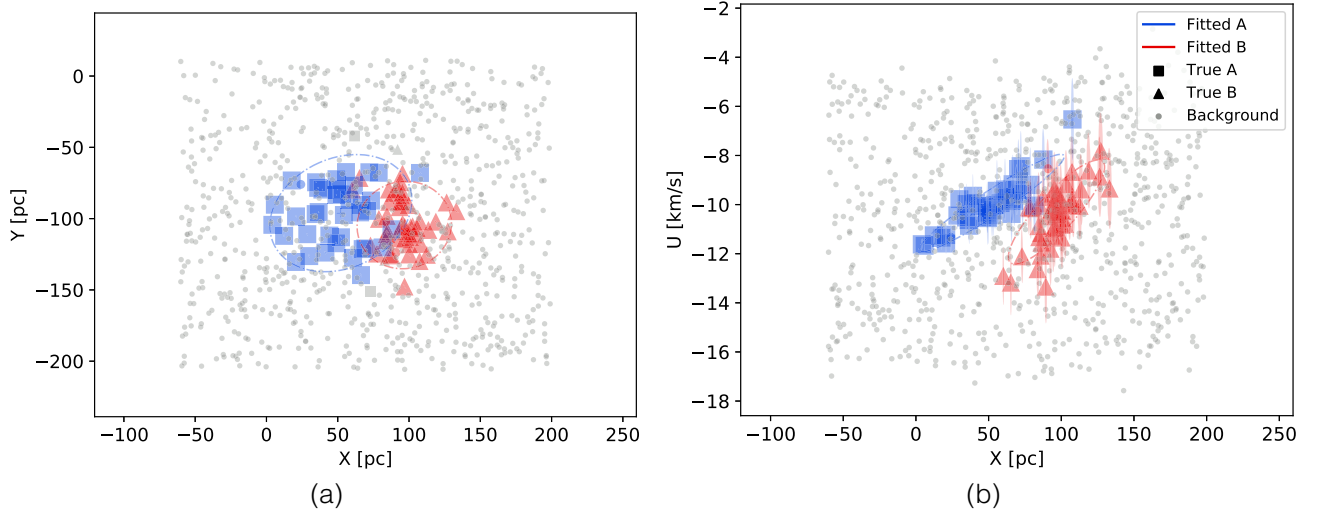
Figure 8. Results from our test using two components combined with a fixed, uniform background. See caption to Fig. 6 for an explanation for figure details. The grey circles show positions of background stars that are correctly classified as part of the background. The grey square and triangular markers show stars that are in fact part of one of the two components of the association, but that are incorrectly classified as part of the background by `Chronostar`. There are only five such markers, because `Chronostar` correctly classifies 85 (of 90) component stars.

Table 7. Astrometry and memberships to βPMG (Comp A) as well as reference to previous work listing star as member of βPMG. Full table available in machine-readable format in online version.

Main Designation	R.A. (deg)	Decl (deg)	Parallax (mas)	$\mu_\alpha\cos\delta$ (mas yr^{-1})	μ_δ (mas yr^{-1})	RV (km s^{-1})	Comp. A Memb. Prob.	RV ref	Prev. βPMG ref
HD 203	1.709	−23.108	25.02 ± 0.06	96.8 ± 0.1	−47.12 ± 0.07	7 ± 4	0.9836	20	1
RBS 38	4.349	−66.753	27.17 ± 0.03	103.04 ± 0.05	−16.87 ± 0.05	10.7 ± 0.2	0.99927	21	1
GJ 2006 A	6.960	−32.552	28.66 ± 0.07	109.8 ± 0.1	−47.39 ± 0.07	8.8 ± 0.2	0.99731	21	1
| GJ 2006 B	6.960	−32.557	28.68 ± 0.08	112.2 ± 0.1	−44.64 ± 0.07	8.5 ± 0.2	–	21	1
Barta 161 12	23.808	−7.215	26.82 ± 0.09	97.5 ± 0.2	−49.09 ± 0.09	6.8 ± 0.8	0.93598	21	1
G 271-110	24.231	−6.794	41.7 ± 0.1	173.5 ± 0.3	−100.1 ± 0.2	12.2 ± 0.4	0.0	27	1
HD 14082 A	34.356	28.745	25.13 ± 0.04	86.92 ± 0.07	−74.07 ± 0.07	5.4 ± 0.5	0.89691	22	1
| HD 14082 B	34.353	28.741	25.16 ± 0.05	85.97 ± 0.08	−71.11 ± 0.08	4.7 ± 0.2	–	15	1
AG Tri A	36.872	30.973	24.36 ± 0.05	79.68 ± 0.08	−72.00 ± 0.07	4.8 ± 0.1	0.8783	15	1
| AG Tri B	36.867	30.978	24.45 ± 0.08	82.7 ± 0.1	−73.49 ± 0.09	5 ± 1	–	24	1
BD+05 378	40.358	5.988	22.50 ± 0.08	79.12 ± 0.10	−56.6 ± 0.1	5.7 ± 0.4	0.0	15	1

Note. βPMG membership references: (1) Gagné et al. (2018b), (2) Schlieder, Lépine & Simon (2010), (3) Alonso-Floriano et al. (2015), (4) Moor et al. (2006), (5) Elliott et al. (2014), (6) Moór et al. (2013), (7) Torres et al. (2008), (8) Gagné et al. (2018c), (9) Zuckerman et al. (2001), (10) Malo et al. (2013), (11) Malo et al. (2014), (12) Kiss et al. (2011), (13) Elliott et al. (2016), (29) Gagné & Faherty (2018), (30) Gagné, Faherty & Fontaine (2018a), (31) Neuhäuser & Forbrich (2008). RV references: (14) Torres et al. (2006), (15) Gaia Collaboration et al. (2018), (16) Kiss et al. (2011), (17) Allers et al. (2016), (18) Shkolnik et al. (2017), (19) Torres et al. (2009), (20) Gontcharov (2006), (21) Malo et al. (2014), (22) Valenti & Fischer (2005), (23) Anderson & Francis (2012), (24) Song et al. (2003), (25) Montes et al. (2001), (26) Kharchenko et al. (2007), (27) Shkolnik et al. (2012), (28) Faherty et al. (2016).

lacking measurements with placeholder values with extremely large uncertainties.

We next extend our list by adding stars from the *Gaia* DR2 catalogue that have not been identified as βPMG members by BANYAN, but are none the less nearby in phase-space. To accomplish this, we draw a box in 6D phase-space around the centre of the BANYAN stellar list, with its size chosen to be twice the span of the BANYAN stars in each dimension. The dimensions of this box are $X = (-84.6, 133.1)$ pc, $Y = (-60.8, 47.3)$ pc, $Z = (-34.3, 45.9)$ pc, $U = (-7.1, 9.5)$ km s^{-1}, $V = (-9.4, 2.0)$ km s^{-1}, and $W = (-8.5, 7.5)$ km s^{-1}. We add to our star list all *Gaia* DR2 stars whose central estimates of position and velocity fall within this box, and which are not already in the BANYAN list. Our final stellar list consists of 859 stars, of which 52 are from the BANYAN catalogue and 807 are nearby *Gaia* DR2 stars that have not been identified as βPMG members by BANYAN.

Our final data preparation step is to handle binary and multiple star systems. The velocities of these stars may contain a large contribution from their orbital motion, and thus even if the centre of mass velocity of a binary system is consistent with being a group member, the component stars may be falsely flagged as non-members because their velocities are inconsistent with that of the group. To avoid this problem, whenever possible we replace multiple star systems with a single pseudo-star whose position and velocity (and the associated uncertainties on these quantities) are mass-weighted averages of the values for the individual stars in the multiple system. For stars in the BANYAN catalogue that are flagged as multiple, we compute the mass-weighted average by converting their spectral types (also taken from the BANYAN catalogue) to masses using the conversion table provided by Kraus & Hillenbrand (2007). Unfortunately we cannot make a similar correction for *Gaia* DR2 stars that are not in the BANYAN catalogue, because we have no
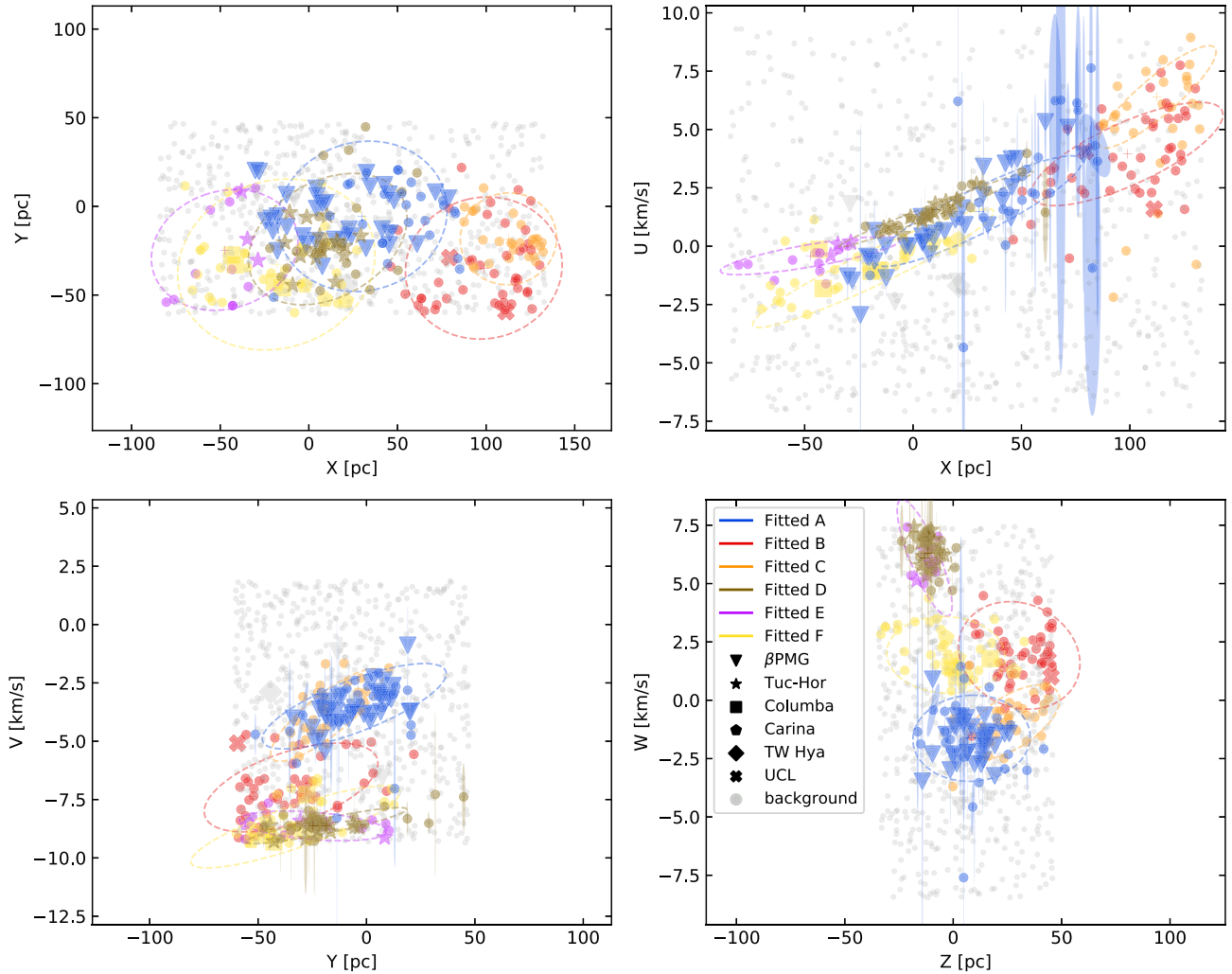
Figure 9. Results from Chronostar's decomposition of stars identified as βPMG members by BANYAN, plus surrounding *Gaia* DR2 stars. Panels show current-day positions and velocities of stars in several different 2D projections. Colours indicate component assignments derived by Chronostar, while marker styles show assignments of stars to groups and associations in the BANYAN catalogue; circles, labelled 'Background' in the legend, are stars not identified as members of any moving group or association by BANYAN, while grey points are stars assigned to the background component by Chronostar. Filled ellipses around the current-day positions show the error distributions for the measurements; for clarity we only show error ellipses for probable members of components A and D. The dashed ellipses show the best-fitting current-day distributions retrieved by Chronostar, coloured by component. Component properties derived by Chronostar are provided in Table 5, while a list of likely βPMG members is given in Table 7.

straightforward method of identifying which of them are members of multiple systems. Consequently, there may be true βPMG members in the *Gaia* DR2 catalogue that are not identified as such by Chronostar because their kinematics are contaminated by orbital motion. However, since these are only false negatives, rather than false positives, we do not expect this effect to substantially influence the overall group properties that we determine. This step merges the 52 BANYAN βPMG members into 38 stars with this change reflected in the following plots.

4.2 Results of the fit

We run Chronostar on the star list constructed as described above. The resulting fit identifies six components, which we denote A through F. We show this decomposition in Fig. 9. Of the six components, A clearly corresponds to the known βPMG; it includes 34 of the 38 stars in the BANYAN βPMG catalogue, along with

an additional 27 members that we discuss in detail below.[7] The estimated age for this component is $17.8 \pm 1.2\,\mathrm{Myr}$; we report this and other fit results in Table 5. The α value for the βPMG component is 50, indicating that perhaps there is mass missing in the form of unidentified members. This component is definitively identified as single by Chronostar: a six-component model that attempts to divide component A from the best five-component into two sub-parts yields a BIC value that is 39 higher (see Table 6 for summary of BIC values across entire run), strongly favouring the six-component fit.

Of the other five components returned by Chronostar, we can identify D with the previously known Tucana-Horologium moving

---

[7]We remind the reader that Chronostar actually returns fractional membership probabilities, so when we refer to a star as being identified as a member of a particular component, we mean that this is the component for which the star has the highest membership probability.

Table 5. Parameters for the βPMG and part of the Tuc-Hor moving group (see the main text) derived by `Chronostar`'s fit to βPMG and nearby *Gaia* DR2 stars (components A and D in Fig. 9, respectively). We suppress here the correlations between dimensions in the covariance matrices, but the full covariance matrices can be found in the online version.

	βPMG		Partial Tuc-Hor	
	Origin	Current	Origin	Current
x (pc)	$33.7^{+3.8}_{-3.4}$	$30.0^{+3.2}_{-3.1}$	$232.0^{+16.4}_{-16.5}$	$12.0^{+3.6}_{-3.6}$
y (pc)	$46.6^{+3.3}_{-3.2}$	$-5.5^{+2.8}_{-2.8}$	$155.8^{+5.3}_{-6.4}$	$-17.2^{+3.0}_{-3.0}$
z (pc)	$22.2^{+1.9}_{-1.8}$	$7.5^{+1.7}_{-1.7}$	$-20.1^{+8.7}_{-8.6}$	$-11.8^{+0.9}_{-0.8}$
u (km s^{-1})	$-0.7^{+0.2}_{-0.2}$	$1.5^{+0.2}_{-0.2}$	$-7.7^{+0.4}_{-0.4}$	$1.6^{+0.1}_{-0.1}$
v (km s^{-1})	$-3.4^{+0.2}_{-0.2}$	$-3.5^{+0.1}_{-0.1}$	$-2.5^{+0.5}_{-0.5}$	$-8.6^{+0.1}_{-0.1}$
w (km s^{-1})	$0.2^{+0.2}_{-0.2}$	$-1.6^{+0.1}_{-0.1}$	$-6.3^{+0.2}_{-0.2}$	$6.3^{+0.1}_{-0.1}$
σ_x (pc)	$12.8^{+0.9}_{-0.8}$	$24.5^{+1.5}_{-1.4}$	$4.8^{+0.4}_{-0.4}$	$23.2^{+1.7}_{-1.5}$
σ_y (pc)	$12.8^{+0.9}_{-0.8}$	$21.6^{+1.2}_{-1.1}$	$4.8^{+0.4}_{-0.4}$	$19.2^{+1.4}_{-1.2}$
σ_z (pc)	$12.8^{+0.9}_{-0.8}$	$13.7^{+0.9}_{-0.8}$	$4.8^{+0.4}_{-0.4}$	$5.6^{+0.4}_{-0.4}$
σ_u (km s^{-1})	$1.0^{+0.1}_{-0.1}$	$1.2^{+0.1}_{-0.1}$	$0.53^{+0.04}_{-0.03}$	$0.8^{+0.1}_{-0.1}$
σ_v (km s^{-1})	$1.0^{+0.1}_{-0.1}$	$0.9^{+0.1}_{-0.1}$	$0.53^{+0.04}_{-0.03}$	$0.40^{+0.03}_{-0.02}$
σ_w (km s^{-1})	$1.0^{+0.1}_{-0.1}$	$1.0^{+0.1}_{-0.1}$	$0.53^{+0.04}_{-0.03}$	$0.49^{+0.03}_{-0.03}$
Age (Myr)	–	$17.8^{+1.2}_{-1.2}$	–	$36.3^{+1.3}_{-1.4}$
nstars	–	59.3	–	41.1

group: of the 46 stars identified as members of this component, 17 are listed as Tucana-Horologium members in the BANYAN catalogue (Gagné et al. 2018c). Our age estimate for this component is $36.3^{+1.3}_{-1.4}$ Myr which is consistent with the LDB age estimate of ≈40 Myr given by Kraus et al. (2014). We report this and other fit parameters for Tuc-Hor in Table 5. However, we warn that, because the component that we identify with Tuc-Hor lies at the edge of the selection box used to construct our stellar list, and thus a substantial number of Tuc-Hor stars are missing from our input stellar list, the recovered position and velocity should be regarded as unreliable. The slopes in phase-space, and thus the age, are more robust to incomplete data. Independent of this issue, we emphasize that `Chronostar`'s identification of Tuc-Hor represents a true, blind discovery of an association in the *Gaia* DR2 data, since our input stellar list was not in any way selected to favour known Tuc-Hor stars.

The remaining four components identified by `Chronostar` do not obviously correspond to any known associations. Because these components, like Tuc-Hor, lie at the edge of our sample selection box, and because unlike Tuc-Hor there is at present no evidence
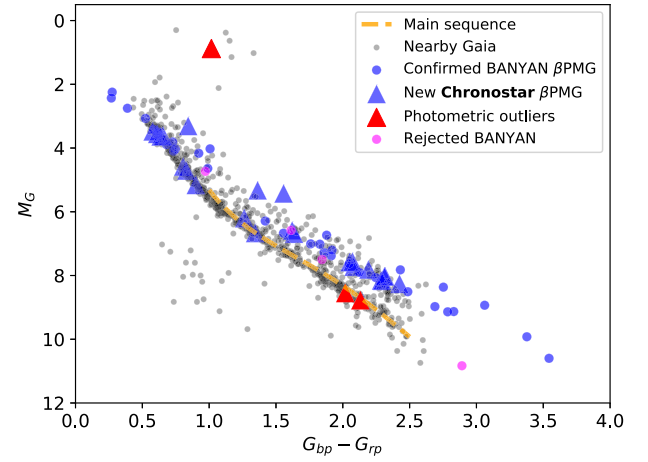

Figure 10. Colour-magnitude diagram of our fit to βPMG, featuring all stars in the set described by Section 4.1. The grey dots are background *Gaia* stars, with a clear clustering on the main sequence. The dashed orange line is an empirical fit to the main sequence. The blue markers denote βPMG members according to `Chronostar`. Stars that are also βPMG members according to BANYAN have circle markers, while those that are new members have triangle markers. BANYAN members that are rejected by `Chronostar` are shown as pink circles. The three `Chronostar` members that appear photometrically inconsistent are coloured red.

that these stellar groups are truly coeval, we do not consider their properties reliable at this point. We defer further investigation of these components to future work.

4.3 New βPMG members

Component A of the `Chronostar` decomposition, which we identify with the βPMG, has 61 stars with membership probabilities greater than 50 per cent (46 greater than 90 per cent). Of these, 34 are identified by BANYAN as βPMG members. Five further stars are classified as βPMG members in follow up BANYAN papers (Gagné & Faherty 2018; Gagné et al. 2018b; Gagné, Faherty & Mamajek 2018d), and nine have been identified as likely βPMG members by other authors (see Table 5 for references), leaving 13 stars identified by `Chronostar` as likely βPMG members for the first time. A colour magnitude diagram (Fig. 10) reveals that 10 of these 13 are consistent with lying on an isochrone that is substantially above the main sequence formed by the background stars and consistent with an isochrone formed by previously identified βPMG members, further supporting their identification. Thus the Bayesian forward-

Table 6. The BICs scored by various multicomponent fits to βPMG. Each column has an entry for each unique initialization for the given number of components. In each column the lowest BIC (in bold) is taken as the best fit for the given component count. The fit that yielded this BIC is then used to initialize multiple fits with $n + 1$ components. The row denotes which component from the previous best fit Chronostar decomposes. For example, `Chronostar` performed two three-component fits, initializing the first by decomposing Component A of the two-component result. `Chronostar` initialized the second by decomposing Component B, which yielded a better BIC. `Chronostar` terminated with six components because all of the attempted seven component fits failed to improve the BIC.

	1 Comp	2 Comps	3 Comps	4 Comps	5 Comps	6 Comps	7 Comps
Comp A	**28 702.90**	**27 984.69**	28 311.91	**27 505.76**	27 566.69	27 501.87	27 479.64
Comp B	–	–	**27 752.75**	27 818.54	**27 449.76**	27 489.28	27 481.18
Comp C	–	–	–	27 761.06	27 558.12	27 449.33	27 506.65
Comp D	–	–	–	**–**	27 563.82	27 481.90	27 494.94
Comp E	–	–	–	–	–	**27 440.57**	27 500.21
Comp F	–	–	–	–	–	–	**27 448.21**

modelling method of `Chronostar`, coupled with the quality of *Gaia* DR2, has allowed us to expand the list of known βPMG members by about 20 per cent.

Most of the newly identified βPMG stars have large *X* and *U*, indicating that the βPMG extends further in *X* (towards the Galactic Centre) than previously thought. These stars were likely missed in previous surveys because their greater distances imply larger astrometric uncertainties. The reason we are able to identify these stars at likely members, while previous studies missed them, is that `Chronostar`'s forward-modelling method is significantly more robust against uncertainties than earlier traceback methods.

5 DISCUSSION

In this paper we have described the `Chronostar` method for kinematic age estimation and membership classification of unbound stellar associations. `Chronostar` models an initial association component as a 6D Gaussian with uncorrelated positions and velocities, projects this forwards in the Galactic potential and maximizes the likelihood of the component parameters by overlap with current-day stellar measurements. Multiple components are treated with an expectation maximization (EM) algorithm, and individual components have a physical, virial prior on position and velocity dispersions. This approach differs from Rizzuto, Ireland & Robertson (2011) and BANYAN (Gagné et al. 2018c), which do not consider time evolution, and differs from LACEwING (Riedel et al. 2017) and Miret-Roig et al. (2018), which trace stellar measurements backwards through time.

The first distinguishing feature of `Chronostar` is how it handles kinematic fitting and membership assignment in a self-consistent way, treating the two aspects as a single problem, and iterating through their circular dependency until convergence. Other approaches (e.g. BANYAN, LACEwING) derive association parameters from pre-defined membership lists, which in effect (after potential removal of suspected interlopers) restricts the discovery of new members to the vicinity of known members. This also impedes applying constraints on the current-day distributions of associations based on what is physically plausible. For example, the classical decomposition of the Scorpius Centaurus OB association into three sub-groups has minimal physical justification (Rizzuto et al. 2011), and indeed impedes kinematic ageing techniques when performed on the large-scale structure enforced by this classification (Wright & Mamajek 2018).

The second significant difference is `Chronostar`'s forward modelling of an initial, compact distribution through the Galactic potential to its current-day distribution, intrinsically anchoring the various variances and covariances of all dimensions of the 6D ellipsoid to the modelled age. One obvious benefit of this approach is the provision of kinematic ages. A second and less obvious benefit is that the tight position–velocity correlations induced by the motions of stars through the Galactic potential allow us to more confidently reject interlopers that fall well within the extent of the distribution of association members in one or more dimensions (position or velocity), but do not lie on the correct position–velocity correlation. This approach is similar to the principle behind expansion ages (e.g. Torres et al. 2008; Wright & Mamajek 2018), but whereas past applications assume linear expansion, `Chronostar` accounts for the effects of the Galactic potential on stellar orbits. This difference is crucial in pushing to ages $\gtrsim 10-20$ Myr, because the vertical oscillation period of stars through the Galactic plane is ≈ 80 Myr (74 Myr in our model of the Galactic potential, and 87 ± 4 Myr using

Oort constants from Bovy 2017). Position–velocity correlations rotate $90°$ in the $Z-W$ plane over a quarter period (c.f. the discussion in Section 3.1), so the assumption of purely linear expansion begins to fail seriously after only $\approx 10-20$ Myr. A third benefit to forward modelling as done in `Chronostar` is that it is considerably more robust than traceback or similar methods against observational uncertainties. Typical radial velocity errors are ≈ 1 km s^{-1} (e.g. Kraus & Hillenbrand 2008), comparable to the intrinsic velocity dispersions of associations. As a result, as one attempts to trace stars backward, the volume of possible stellar positions balloons rapidly. Attempts to sample this volume using Monte Carlo or similar techniques have thus far proven relatively unsuccessful at delivering reliable kinematic ages (e.g. Donaldson et al. 2016; Riedel et al. 2017; Miret-Roig et al. 2018). In contrast, trace-forward combined with analysis of the overlap between a proposed association and observed stars in 6D phase-space does not suffer from this explosion of possibilities, because the phase-space volume occupied by a proposed stellar distribution is conserved as one traces it forward.

6 CONCLUSION AND FUTURE WORK

In this paper we have presented the methodology for `Chronostar`, a new kinematic analysis tool to identify and age unbound stars that share a common origin. The tool requires no manual calibration or pre-selection, and simultaneously and self-consistently solves the problems of assigning stars to associations and determining the properties of those associations. We test `Chronostar` extensively on synthetic data sets, including ones containing multiple, overlapping components and ones where the initial positions and velocities are stars are drawn directly from a hydrodynamic simulation of star formation, and show that it returns very accurate membership assignments and kinematic ages. In tests on real data, we show that `Chronostar` is capable of blindly recovering the β Pictoris and Tucana-Horologium moving groups (Fig. 9), with the kinematic data used to find the latter originating solely from *Gaia* DR2. In the future we intend to apply `Chronostar` to other known associations, with incorporated radial velocities from dedicated spectroscopic surveys (i.e. RAVE, Kunder et al. 2017; GALAH, Buder et al. 2018). This should for the first time provide reliable kinematic ages. Since `Chronostar` has proven to be capable of blind discovery, we also intend to search the phase-space near the Sun for previously unknown associations.

Due to the Bayesian nature of `Chronostar`, it is also straightforward to extend it by adding extra dimensions to the parameter space for even stronger membership classification. This includes placing priors on the ages of individual stars based on spectroscopic types, and incorporating chemical tagging into the fitting mechanism. Two further possible enhancements that we intend to pursue in future work include allowing for the possibility that associations might be born with significant position–velocity correlations (as suggested for example by Tobin et al. 2009 and Offner, Hansen & Krumholz 2009), and allowing `Chronostar` to fit not only unbound associations but also bound open clusters that are slowly evaporating.

REFERENCES

Allers K. N., Gallimore J. F., Liu M. C., Dupuy T. J., 2016, ApJ, 819, 133
Alonso-Floriano F. J., Caballero J. A., Cortés-Contreras M., Solano E., Montes D., 2015, A&A, 583, A85
Anderson E., Francis C., 2012, Astron. Lett., 38, 331
Bovy J., 2015, ApJS, 216, 29
Bovy J., 2017, MNRAS, 468, L63
Buder S. et al., 2018, MNRAS, 478, 4513
Donaldson J. K., Weinberger A. J., Gagné J., Faherty J. K., Boss A. P., Keiser S. A., 2016, ApJ, 833, 95
Ducourant C., Teixeira R., Galli P. A. B., Le Campion J. F., Krone-Martins A., Zuckerman B., Chauvin G., Song I., 2014, A&A, 563, A121
Elliott P., Bayo A., Melo C. H. F., Torres C. A. O., Sterzik M., Quast G. R., 2014, A&A, 568, A26
Elliott P., Bayo A., Melo C. H. F., Torres C. A. O., Sterzik M. F., Quast G. R., Montes D., Brahm R., 2016, A&A, 590, A13
Faherty J. K. et al., 2016, ApJS, 225, 10
Federrath C., 2015, MNRAS, 450, 4035
Federrath C., Krumholz M., Hopkins P. F., 2017, J. Phys.: Conf. Ser., 837, 012007
Foreman-Mackey D., Hogg D. W., Lang D., Goodman J., 2013, PASP, 125, 306
Gagné J., Faherty J. K., 2018, ApJ, 862, 138
Gagné J., Faherty J. K., Fontaine G., 2018a, Res. Notes Am. Astron. Soc., 2, 9
Gagné J. et al., 2018b, ApJ, 856, 23
Gagné J., Roy-Loubier O., Faherty J. K., Doyon R., Malo L., 2018c, ApJ, 860, 43
Gagné J., Faherty J. K., Mamajek E. E., 2018d, ApJ, 865, 136
Gaia Collaboration, 2018, A&A, 616, A11
Gontcharov G. A., 2006, Astron. Lett., 32, 759
Johnson D. R. H., Soderblom D. R., 1987, AJ, 93, 864
Jones E., Oliphant T. E., Peterson P. et al., 2001, SciPy: Open Source Scientific Tools for Python. Available at: http://www.scipy.org/
Kharchenko N. V., Scholz R.-D., Piskunov A. E., Röser S., Schilbach E., 2007, Astron. Nachr., 328, 889
Kiss L. L. et al., 2011, MNRAS, 411, 117
Kraus A. L., Hillenbrand L. A., 2007, AJ, 134, 2340
Kraus A. L., Hillenbrand L. A., 2008, ApJ, 686, L111
Kraus A. L., Shkolnik E. L., Allers K. N., Liu M. C., 2014, AJ, 147, 146
Kunder A. et al., 2017, AJ, 153, 75
Makarov V. V., 2007, ApJS, 169, 105
Malo L., Doyon R., Lafrenière D., Artigau É., Gagné J., Baron F., Riedel A., 2013, ApJ, 762, 88
Malo L., Artigau É., Doyon R., Lafrenière D., Albert L., Gagné J., 2014, ApJ, 788, 81
Mamajek E. E., Bell C. P. M., 2014, MNRAS, 445, 2169
McLachlan G., Peel D., 2004, Finite Mixture Models. John Wiley & Sons, Hoboken, NJ.
Miret-Roig N., Antoja T., Romero-Gómez M., Figueras F., 2018, A&A, 615, A51
Montes D., López-Santiago J., Gálvez M. C., Fernández-Figueroa M. J., De Castro E., Cornide M., 2001, MNRAS, 328, 45
Moór A., Ábrahám P., Derekas A., Kiss C., Kiss L. L., Apai D., Grady C., Henning T., 2006, ApJ, 644, 525
Moór A., Szabó G. M., Kiss L. L., Kiss C., Ábrahám P., Szulágyi J., Kóspál Á., Szalai T., 2013, MNRAS, 435, 1376
Neuhäuser R., Forbrich J., 2008, in Reipurth B., ed., Handbook of Star Forming Regions, Volume II. The Southern Sky. ASP Monograph Publ., San Francisco, CA, p. 735
Offner S. S. R., Hansen C. E., Krumholz M. R., 2009, ApJ, 704, L124
Onus A., Krumholz M. R., Federrath C., 2018, MNRAS, 479, 1702
Ortega V. G., de la Reza R., Jilinski E., Bazzanella B., 2002, ApJ, 575, L75
Ortega V. G., de la Reza R., Jilinski E., Bazzanella B., 2004, ApJ, 609, 243
Riedel A. R., Blunt S. C., Lambrides E. L., Rice E. L., Cruz K. L., Faherty J. K., 2017, AJ, 153, 95
Rizzuto A. C., Ireland M. J., Robertson J. G., 2011, MNRAS, 416, 3108
Rizzuto A. C., Ireland M. J., Kraus A. L., 2015, MNRAS, 448, 2737
Schlieder J. E., Lépine S., Simon M., 2010, AJ, 140, 119
Schwarz G., 1978, Ann. Stat., 6, 461
Schönrich R., Binney J., Dehnen W., 2010, MNRAS, 403, 1829
Scott D. W., 1992, Multivariate Density Estimation: Theory, Practice, and Visualization. Wiley, Hoboken, NJ
Shkolnik E. L., Anglada-Escudé G., Liu M. C., Bowler B. P., Weinberger A. J., Boss A. P., Reid I. N., Tamura M., 2012, ApJ, 758, 56
Shkolnik E. L., Allers K. N., Kraus A. L., Liu M. C., Flagg L., 2017, AJ, 154, 69
Song I., Zuckerman B., Bessell M. S., 2003, ApJ, 599, 342
Tobin J. J., Hartmann L., Furesz G., Mateo M., Megeath S. T., 2009, ApJ, 697, 1103
Torres C. A. O., Quast G. R., Melo C. H. F., Sterzik M. F., 2008, in Reipurth B., ed., Handbook of Star Forming Regions, Volume II, The Southern Sky. ASP Monograph Publ., San Francisco, CA, p. 757
Torres C. A. O., Quast G. R., da Silva L., de La Reza R., Melo C. H. F., Sterzik M., 2006, A&A, 460, 695
Torres R. M., Loinard L., Mioduszewski A. J., Rodríguez L. F., 2009, ApJ, 698, 242
Valenti J. A., Fischer D. A., 2005, ApJS, 159, 141
Wright N. J., Mamajek E. E., 2018, MNRAS, 476, 381
Zuckerman B., Song I., Bessell M. S., Webb R. A., 2001, ApJ, 562, L87

SUPPORTING INFORMATION

Supplementary data are available at *MNRAS* online.

Table 7. Astrometry and memberships to βPMG (Comp A) as well as reference to previous work listing star as member of βPMG.

Please note: Oxford University Press is not responsible for the content or functionality of any supporting materials supplied by the authors. Any queries (other than missing material) should be directed to the corresponding author for the article.

APPENDIX A: PROJECTING A COMPONENT THROUGH TIME

This appendix details our method of taking a component's initial distribution in 6D phase-space $\mathcal{N}(\boldsymbol{\theta}; \mu_0, \Sigma_0)$ and, using GALPY's orbit calculations (Bovy 2015), projecting it forward through time by its modelled age t_c to its current-day distribution $\mathcal{N}(\boldsymbol{\theta}; \mu_c, \Sigma_c)$.

The technical details of the implementation used by galpy[8] to calculate orbits are irrelevant for our method so we abstract the galpy orbit calculation as a function **f** that maps a starting point $\boldsymbol{\theta}_0$ in the 6D phase-space forward over an arbitrary time to a new point $\boldsymbol{\theta}_f$. Thus we use **f** to project μ_0 and Σ_0 to their current-day values, μ_c and Σ_c. Acquiring the current-day central value is simply

---

[8]We used the integrator option 'odeint' which utilizes scipy's odeint.

a matter of evolving the initial central point forward by the modelled age. In our abstracting notation this reads:

$$\boldsymbol{\mu}_c = \mathbf{f}(\boldsymbol{\mu}_0, t_c).$$ (A1)

To transform the covariance matrix $\boldsymbol{\Sigma}_0$ it is useful to think in terms of a coordinate transformation between two systems: the initial coordinates, and the current-day coordinates. To linear order, the covariance matrix $\boldsymbol{\Sigma}_B$ in the new coordinate system B is given by the usual law for error propagation,

$$\boldsymbol{\Sigma}_B = \mathbf{J}_A \boldsymbol{\Sigma}_A \mathbf{J}_A^T,$$ (A2)

where $\boldsymbol{\Sigma}_A$ is the covariance matrix in the original coordinates A, and $\mathbf{J}$ is the Jacobian for the mapping between the two coordinate systems; specifically, if some function $\mathbf{g}(\mathbf{a})$ maps a point $\mathbf{a}$ in coordinate system A to a corresponding point in B, then $\mathbf{J}_{ij} = \partial g_i / \partial a_j$.

In our case of orbit evolution, the mapping function $\mathbf{g}$ is simply $\mathbf{f}(\boldsymbol{\mu}_0, t_c)$, and thus the Jacobian evaluated at starting phase-space position $\boldsymbol{\mu}_0$ is

$$\mathbf{J}_{ij} = \frac{\partial}{\partial \theta_{0,j}} \left(f(\mu_0, t_c)_i \right) = \frac{\partial \theta_{c,i}}{\partial \theta_{0,j}},$$ (A3)

where $\theta_{0,i}$ and $\theta_{c,i}$ are the ith components of $\boldsymbol{\mu}_0$ and $\boldsymbol{\mu}_c = \mathbf{f}(\boldsymbol{\mu}_0, t_c)$, respectively. That is, $\theta_{0,i}$ and $\theta_{c,i}$ are the ith components of the phase-space coordinates of the association's centre at the time of its birth and at the current time, respectively. We cannot evaluate the Jacobian $\mathbf{J}$ analytically because evaluation of $\mathbf{f}$ requires numerical integration of an orbit through the Galactic potential. Instead, we evaluate the partial derivatives numerically using a second-order approximation:

$$\frac{\partial \theta_{c,i}}{\partial \theta_{0,j}} \approx \frac{f(\boldsymbol{\theta}_0 + \boldsymbol{h}, t)_i - f(\boldsymbol{\theta}_0 - \boldsymbol{h}, t)_i}{2|h|},$$ (A4)

where $\boldsymbol{h}$ is a 6D vector with $h_j = 10^{-5}$ (pc or km s^{-1}, depending on dimension) and all other components zero.

One might worry about the numerical stability of this procedure, and this would indeed be a concern if the potential through which we were integrating the orbits were tabulated numerically, or contained significant small-scale structure. However, our potential is both analytic and very smooth, and as a result both the orbit integration and the numerical derivative returned by equation (A4) are extremely robust to changes in h as long as all components of $\boldsymbol{h}$

are much smaller than the size scale on which the potential varies, and much larger than the $\approx 10^{-8}$ error tolerance in the numerical integrator. To confirm this directly, we have experimented with varying h from 10^{-1} to 10^{-6}. We find that, over this range, the non-zero components of $\partial \theta_{c,i} / \partial \theta_{0,j}$ vary by < 0.01 per cent in the vast majority of cases, and by < 1 per cent in all cases.

APPENDIX B: EXPLORING DEPENDENCE ON POTENTIAL MODEL

The choice of the potential model influences the calculated orbits and thus the resulting age fits. To explore the dependence we repeat the test described in Section 3.3.2 using two different potential models. In both cases we use the same synthetic data which we generated using the potential model `MWPotential2014`, but then use `Chronostar` to fit the stellar population using a different potential, in order to determine how sensitive our results are to uncertainties in the potential.

The two key time-scales of our potential model are the vertical oscillation frequency and the epicyclic frequency. We expect the vertical oscillation period to have the greater effect on the age fit as this is the shorter time-scale by a factor of 2. Therefore in the two following tests we alter the potential by varying the scale height of the disc component. In the first test we halve the scale height, and in the second we double it. These new potentials have vertical oscillation periods scaled by 0.73 and 1.33, respectively.

Fitting the synthetic data described in Section 3.3.2 using a potential with a halved scale height continues to yield two components, with estimated ages of $6.8^{+0.2}_{-0.1}$ and $9.9^{+0.1}_{-0.2}$ Myr. The corresponding results for a potential with a doubled scale height are 6.8 ± 0.1 and 9.9 ± 0.1 Myr. These compare well with the true ages of 7 and 10 Myr, and with the ages determined using the correct potential. Thus, despite the vertical oscillation frequency differing significantly in these two tests, and thus distorting the best fit in the $Z-W$ plane, there is sufficient constraining information in the remaining dimensions to accurately retrieve the ages. The implication of this test is that our age estimates are relatively robust to errors in any particular dimension of the potential.

This paper has been typeset from a TEX/LATEX file prepared by the author.